BSGF
Earth Sciences Bulletin

OPEN ∂ ACCESS

Discovery of Variscan orogenic peridotites in the Pelvoux Massif (Western Alps, France)

Jean-Baptiste Jacob[1,2,*] , Emilie Janots[1], Carole Cordier[1] and Stéphane Guillot[1]

[1] Univ. Grenoble Alpes, Univ. Savoie Mont Blanc, CNRS, IRD, Univ. Gustave Eifel, ISTerre, 38000 Grenoble, France
[2] The Njord Centre, Department of Geoscience, University of Oslo, Oslo, Norway

Abstract – Small bodies of mantle-derived peridotites and other ultramafic rocks are commonly found in exhumed lower crustal units of collisional orogens. They provide a direct record of the complex evolution of the upper mantle before and during an orogeny, and are therefore key markers of the geodynamic evolution of an orogen. We report here the discovery of such mantle-derived peridotites, which occur as fragmented enclaves in migmatites of the high-grade Variscan lower crust exposed in the Pelvoux Massif (external Western Alps). A wide petrographic diversity has been observed, from very fertile, garnet-bearing lherzolites, to more depleted spinel/chromite-bearing harzburgites. Thermobarometric calculations on a garnet lherzolite indicate an initial stage at 3.0–4.0 GPa and 970–1140 °C, followed by exhumation to 0.8–1.3 GPa and 800–850 °C, while the harzburgites do not show any evidence of equilibration in the garnet field. Petrological observations, whole-rock geochemistry and *in situ* mineral compositions suggest the peridotites have undergone a complex history prior to their incorporation in the lower crust during the Variscan Orogeny. They derive from a refractory mantle, which has experienced variable degrees of melt depletion, and has then been extensively refertilized. Cryptic metasomatism is observed in all samples. It is characterized by an enrichment in large-ion lithophile elements (LILE, in particular Cs, Rb, U and Pb) relative to high field strength elements (HFSE), in particular Nb and Ta. This cryptic metasomatism is presumably related to percolation of subduction-related fluids or melts in the mantle. In addition, modal metasomatism occurred in some samples, where crystallization of phlogopite, pargasite, chromite and apatite has been observed. This modal metasomatism resulted in significant enrichment in K_2O, P_2O_5 and Cr_2O_3 of the bulk rock, together with a strong enrichment in incompatible LREE relative to HREE. These geochemical characteristics are strikingly similar to that of syn-collisional, Mg–Cr–LILE rich mantle-derived (ultra)-potassic magmas such as durbachites and vaugnerites, which are ubiquitous in the Variscan metamorphic allochthons of Massif Central, external Alps, Vosges and Bohemian Massif. We therefore suggest that this metasomatism results from dynamic percolation of the peridotites by $K_2O–P_2O_5–Cr_2O_3$-rich melts from which the durbachites and vaugnerites are primarily derived. These geochemical characteristics are in line with whole-rock Nd isotopic compositions, which indicate enrichment of the mantle by a continental crust component, presumably related to Variscan subductions. This evolution is consistent with that of other Variscan peridotites in the Eastern Alps (Ulten) and the Bohemian Massif, where multiple metasomatic episodes related to melts or fluids released in Variscan subduction zones have been documented.

Keywords: orogenic peridotites / cryptic metasomatism / modal metasomatism / mantle refertilization / melt-peridotite interaction / Variscan Belt

Résumé – Découverte de péridotites orogéniques varisques dans le massif du Pelvoux (Alpes occidentales, France). Les unités de croûte inférieure exhumées au sein des orogènes collisionnels contiennent fréquemment des petits corps de péridotite et d'autres roches ultramafiques. Ces roches sont des marqueurs clés de l'évolution géodynamique d'un orogène, car elles fournissent un enregistrement direct de l'évolution du manteau avant et au cours des phases orogéniques. Nous rapportons ici la découverte de péridotites orogéniques au sein d'unités de croûte inférieure varisque, dans le massif du Pelvoux (Alpes occidentales externes). Celles-ci se présentent sous forme d'enclaves fragmentées, emballées dans des

*Corresponding author: j.b.jacob@mn.uio.no

migmatites. On observe une grande diversité pétrographique, allant de lherzolites à grenat très fertile à des harzburgites à spinelle/chromite plus appauvries. Les estimations thermobarométriques effectués sur une lherzolite à grenat indiquent un stade initial à 3,0–4,0 GPa et 970–1140 °C, suivi d'une exhumation à 0,8–1,3 GPa et 800–850 °C, tandis que les harzburgites ne montrent aucune trace d'équilibration dans le champ du grenat. Les observations pétrographiques, les données géochimiques sur roche totale et les compositions minérales *in situ* indiquent que les péridotites ont enregistré une histoire complexe, précédant leur incorporation dans la croûte inférieure au cours de l'orogenèse Varisque. Elles dérivent de domaines mantelliques réfractaires, qui ont subi différents degrés de fusion partielle avant d'être refertilisés. Un métasomatisme cryptique est observé dans tous les échantillons. Il est caractérisé par un enrichissement en éléments lithophiles (en particulier en Cs, Rb, U, Pb) par rapport aux HFSE (*High Field Strength Elements*), en particulier Nb et Ta. Ce métasomatisme est vraisemblablement lié à la percolation de fluides / liquides silicatés issu d'un zone de subduction. Par ailleurs, on observe dans certains échantillons un métasomatisme modal, caractérisé par la cristallisation de phlogopite, de pargasite, de chromite et d'apatite ainsi que par un fort enrichissement en LREE (*Light Rare Earth Elements*) incompatibles par rapport aux HREE (*Heavy Rare Earth Elements*). Ces caractéristiques géochimiques sont très similaires à celles des durbachites et des vaugnérites, des séries de roches magmatiques mantelliques (ultra)-potassiques riches en Mg–Cr–LILE, mises en place au Carbonifère moyen à supérieur dans les unités métamorphiques allochthones du massif central, des Vosges, du massif de Bohème, ainsi que dans le socle varisque des Alpes externes. Ceci suggère l'existence d'un lien génétique entre les durbachites et vaugnérites et le métasomatisme modal observé dans les enclaves. Ce dernier pourrait ainsi être lié à la percolation dans le manteau des magmas primaires riches en K_2O–P_2O_5–Cr_2O_3 dont sont issues les durbachites. Ces caractéristiques géochimiques sont en accord avec les compositions isotopiques en Nd, qui indiquent un enrichissement du manteau par du matériel issu de la croûte continentale, vraisemblablement lié aux subductions varisques. Cette évolution est cohérente avec celle d'autres péridotites varisques dans les Alpes orientales (Ulten) et dans le massif de Bohème, où des épisodes métasomatiques liés à la percolation des fluides / liquides magmatiques mantelliques issus des zones de subduction varisques est bien documentée.

Mots clés : péridotites orogéniques / métasomatisme cryptique / métasomatisme modal / refertilisation mantellique / interactions magma-péridotite / chaîne Varisque

1 Introduction

Occurrence of mantle-derived ultramafic slices, lenses or boudins is a common feature of high-grade lower crustal units exposed in collisional orogens worldwide (*e.g.* Brueckner and Medaris, 2000; Nimis and Trommsdorff, 2001; Medaris *et al.*, 2005; Chen *et al.*, 2015; Brueckner, 2018). Although they only represent a tiny fraction of these high-grade units, ultramafic bodies provide extremely valuable information about metasomatic and magmatic processes occurring in the upper mantle during and before an orogeny (Malaspina *et al.*, 2006; Scambelluri *et al.*, 2006; Sapienza *et al.*, 2009; Brueckner *et al.*, 2010; Kubeš *et al.*, 2022). They may also retain pressure-temperature information and thus provide constraints about burial and exhumation of (ultra)-high-pressure (U-HP) units in collision zones. They are therefore crucial markers to constrain the geodynamic evolution of an orogen.

In the Variscan Belt (Fig. 1a), small ultramafic mantle bodies, including garnet peridotites, spinel peridotites and pyroxenites, are found in the metamorphic allochthonous units that form exhumed portions of the lower-to-mid-crustal orogenic root, mainly in the Bohemian Massif (Medaris *et al.*, 2005, 2015; Kubeš *et al.*, 2022), the Vosges–Black Forest Massif (Altherr and Kalt, 1996; Altherr, 2021) and the French Massif Central (Gardien *et al.*, 1990; Godard, 1990). In detail, these mantle bodies are found in exhumed lower to mid-crustal units from different tectonic domains, which record different metamorphic evolutions (Medaris *et al.*, 2005; Lardeaux *et al.*, 2014; Altherr and Soder, 2018). In the

Bohemian Massif, where the largest number of these ultramafic bodies has been found, a distinction has been recognized between peridotite-bearing units exhumed close to the plate interface (Saxo–Thuringian suture) and those exhumed further south, between the former Devonian subduction arc and the Brunia continental backstop (Molda-nubian zone, Schulmann *et al.*, 2009). The former typically record colder peak-P conditions (< 800 °C) and shorter-lived peak-T than the latter, which record peak-P at UHT conditions (850–1050 °C), followed by near-isothermal decompression (Maierová *et al.*, 2021, and references therein). Therefore, these different units correspond to contrasted exhumation mechanisms, and mark different processes within the Variscan collision. While the plate-interface probably correspond to a former subduction *mélange* exhumed in the subduction channel, exhumation of Moldanubian peridotites and other UHP rocks might involve less conventional mechanisms of lower crustal "relamination" (Schulmann, Lexa *et al.*, 2014; Maierová *et al.*, 2018, 2021).

Multiple studies of the mantle-derived fragments have been undertaken in the Bohemian Massif (*e.g.* Medaris *et al.*, 2005, 2015; Ackerman *et al.*, 2020; Kubeš *et al.*, 2022), which may therefore be a good reference site to discuss these processes. In other Variscan Massifs, deep crustal and mantle processes have been comparatively less studied, mainly because of the scarcity of well-preserved mantle bodies. This is particularly the case in the southeastern Variscides, where there is virtually no study on mantle fragments, apart from the garnet peridotites of the Ulten Zone, in the austroalpine
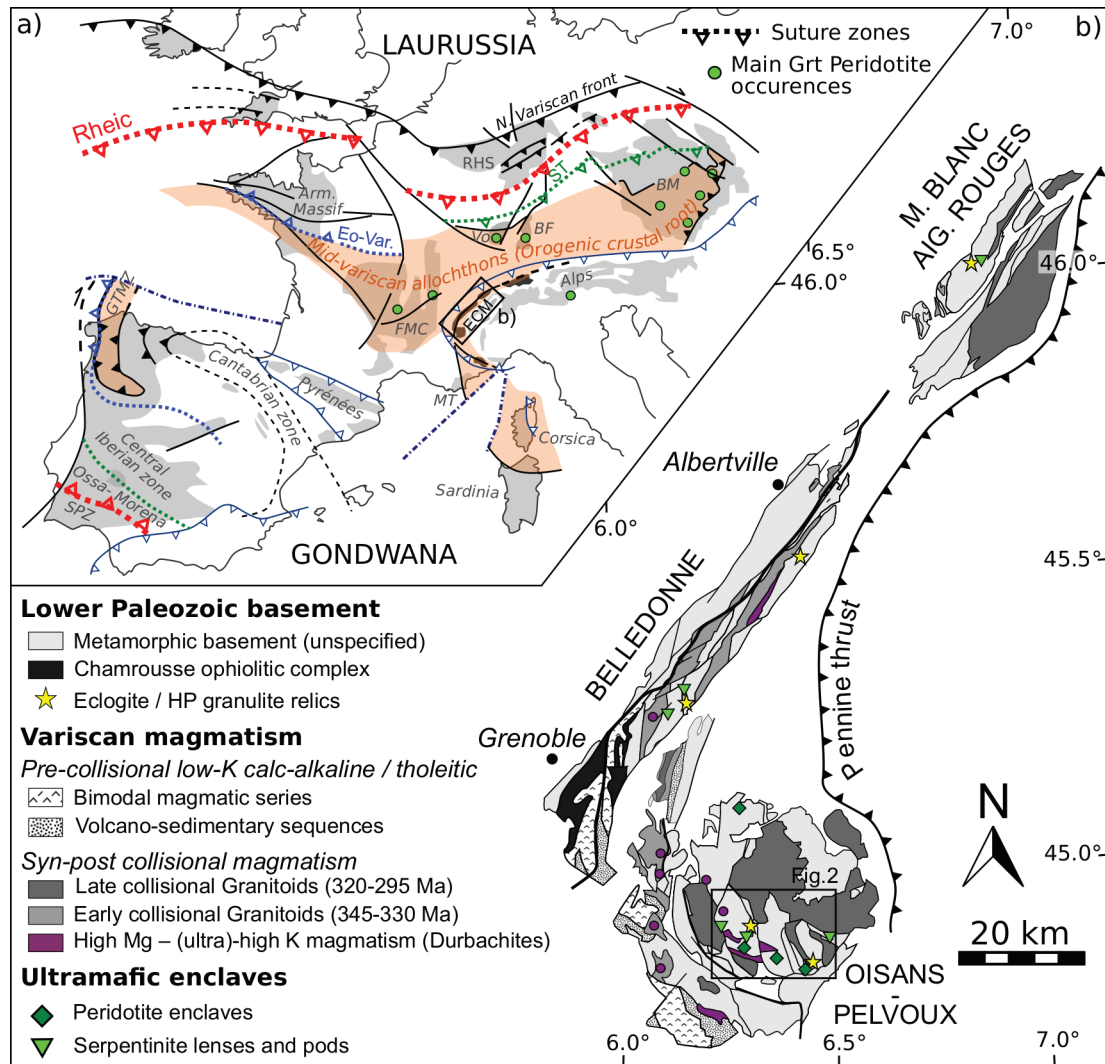
Fig. 1. (a) Location of the External Crystalline Massifs of the Alps in the Variscan Belt. The Mid-Variscan allochthons, which contain portions of the exhumed crustal root, are highlighted in orange. Modified after Ballèvre *et al.* (2014) and Martínez Catalán *et al.* (2021). BF: Black Forest; ECM: External Crystalline Massifs; FMC: French Massif Central; GTMZ: Galicia-Trás-os-Montes; MT: Maures-Tanneron; RHS: Rheinische schiefergebirge; SPZ: South Portugese Zone; ST: Saxo-Thuringian suture; Vo: Vosges. (b) Simplified geological map of the central part of the ECM (Belledonne, Pelvoux, Mont-Blanc and Aiguilles-Rouges), modified from Guillot and Ménot (2009). The investigated area (black rectangle) is located in the central part of Pelvoux Massif (Fig. 2), but two samples of serpentinites were collected in the southern part of Belledonne.

Fig. 1. (a) Localisation des Massifs Crystallins Externes dans la chaîne Varisque. Les unités métamorphiques allochthones (« Mid-Variscan allochthons »), dans lesquels se trouvent les unités de croûte inférieure, sont figurés en orange. Modifié d'après Ballèvre et al. *(2014) et Martínez Catalán* et al. *(2021). BF : Forêt-Noire ; ECM : Massifs Cristallins Externes ; FMC : Massif Central; GTMZ : Galice-Trás-os-Montes ; MT : Maures-Tanneron ; RHS : Rheinische schiefergebirge ; SPZ : Zone sud-portugaise; ST : Suture Saxo-Thuringienne ; Vo : Vosges. (b) Carte géologique simplifiée de la partie centrale des MCE (Belledonne, Pelvoux, Mont-Blanc et Aiguilles-Rouges), modifiée d'après Guillot et Ménot (2009). La zone étudiée (rectangle noir) est située dans la partie centrale du massif de Pelvoux (Fig. 2), mais deux échantillons de serpentinites ont été collectés dans la partie sud de Belledonne.*

basement (Godard *et al.*, 1996; Tumiati *et al.*, 2003; Scambelluri *et al.*, 2006). We document here the discovery of new outcrops of peridotites in the Variscan basement of the external Western Alps, in exhumed lower crustal units of the Pelvoux massif (Fig. 1b). These peridotites occur as fragmented enclaves in migmatites, and some of them have been moderately affected by serpentinization.

This contribution aims to provide field, petrological, thermobarometric, and whole-rock geochemical and isotopic data of these enclaves, in order to discuss their metamorphic and metasomatic evolution. This evolution will then be compared with that of other Variscan mantle bodies, in particular from the Bohemian Massif, in order to provide some insights into the evolution of the Variscan mantle in the external Western Alps.

2 Geological setting

2.1 General setting

The Pelvoux Massif is a well-exposed portion of Variscan middle-to-lower crust located in the French Western Alps (Fig. 1b). It belongs to the External Crystalline Massifs (ECM), which represent the exposed Paleozoic basement in the external Western Alps. The Alpine overprint in these massifs is generally considered to be very mild, and consists mostly in localized brittle/ductile deformation, which occurred at greenschist-facies conditions ($< 350\,°C$, Bellahsen *et al.*, 2014; Bellanger *et al.*, 2015). The Paleozoic basement of the ECM has been strongly overprinted during the Variscan orogeny (Guillot and Ménot, 2009; Jacob *et al.*, 2022), and displays similarities with the metamorphic allochthonous units exposed in the French Massif Central, Vosges and Bohemian Massifs (Faure *et al.*, 2009; Skrzypek *et al.*, 2012; Lardeaux *et al.*, 2014; Vanderhaeghe *et al.*, 2020; Martínez Catalán *et al.*, 2021). This includes in particular: (i) the nature of protoliths, which mainly consist of Cambrian–Ordovician magmatic and sedimentary sequences with widespread tholeitic magmatism, marking a stage of rifting along the northern margin of Gondwana (Von Raumer and Stampfli, 2008); (ii) the presence of ophiolitic relics, the largest one being the ophiolite complex of Chamrousse ($496 \pm 6\,Ma$) in the massif of Belledonne (Pin and Carme, 1987; Ménot *et al.*, 1988), which lies on the top of the metamorphic nappe pile and is devoid of HP metamorphism (Fig. 1b); (iii) the widespread occurrence of (retrogressed) eclogite/ mafic HP granulite bodies in the high-grade lower crustal units. These eclogites record a Visean (ca. 340–330 Ma) HP stage with peak-P conditions estimated around 1.4–1.8 GPa and 650–750 °C (Rubatto *et al.*, 2010; Jouffray *et al.*, 2020; Jacob *et al.*, 2021, 2022; Vanardois *et al.*, 2022). This eclogitisation is interpreted to mark the closure of a short-lived marginal basin opened in a back-arc setting on the Gondwanian plate at ca. 350 Ma (Fréville *et al.*, 2018), which would have been squeezed and incorporated into the Variscan orogenic wedge by southeastward propagation of deformation during the lower to middle Carboniferous (ca. 340–330 Ma). Felsic protoliths do however not record HP conditions. In weakly to non-migmatized gneiss and micaschist of the Western Pelvoux and Belledonne Massif, a Visean (ca. 340–330 Ma) MP–MT stage (0.5–1.0 GPa and 550–680 °C) is recorded, with no relics of HP/UHP assemblages (Guillot and Ménot, 1999; Fréville *et al.*, 2018, 2022). In the more highly migmatized units of inner Pelvoux, this MP–MT stage is overprinted by a HT granulitic stage at ca. 800–850 °C and 0.6–0.9 GPa (Grandjean *et al.*, 1996; Jacob *et al.*, 2022).

As in the rest of the Variscan metamorphic allochthons, Devonian–Carboniferous magmatism is widespread in the ECM. First, the opening of Devonian–Tournaisian basins, presumably in a back-arc setting, was associated with intrusion of trondhjemite dykes and sills around 350 Ma (Fréville *et al.*, 2018). Tonalite plutons of the same age have also been dated in the Aar Massif (Ruiz *et al.*, 2022). This low-K magmatism was followed by emplacement of K-rich sub-alkaline granitoids from the Visean to the early Permian (ca. 345–295 Ma, Debon and Lemmet, 1999). A large part of this magmatism results from crustal anatexis during the syn- to post-collisional stages, as evidenced by the large proportion of migmatized lower crust

exposed in the ECM (Guillot and Ménot, 2009). However, a significant contribution of mantle sources is also evidenced by the presence of (ultra)-potassic (UHK), mafic to intermediate igneous rocks, locally referred to as durbachites or vaugnerites (Debon *et al.*, 1998; Von Raumer *et al.*, 2014). These rocks are particularly rich both in compatible (Mg, Ni, Cr) and incompatible elements including large-ion lithophile elements (LILE: Cs, Rb, Ba, K), Th, U and light rare earth elements (LREE: La, Ce, Nd, Sm). Thus, the most widely accepted view attributes this magmatism to the melting of an enriched, metasomatized mantle source contaminated by subducted crustal material (Janoušek and Holub, 2007; Soder and Romer, 2018).

2.2 The Pelvoux Massif and peridotite-bearing localities

The Pelvoux Massif lies in the eastern part of ECM and exposes high-grade metamorphic series composed of highly migmatized mafic to felsic protoliths (metasediments, orthogneiss, amphibolites), intruded by several granitoid plutons (Fig. 2). The metamorphic series display different sets of N-N150° subvertical and subhorizontal migmatitic foliations, which are consistent with longitudinal flow of partially molten material in a N-N150° sinistral transpressive setting (Fréville *et al.*, 2022; Jacob *et al.*, 2022). However, the early syn-migmatitic fabrics have been partly overprinted by later, sub-solidus deformation occurring in the same sinistral wrenching setting, and by alpine ductile/brittle tectonics (Fig. 2). Occurrence of ultramafic rocks, mainly serpentinites, has been acknowledged for long in the Pelvoux Massif (Pecher, 1970; Le Fort, 1971), as well as in surrounding massifs of Belledonne and Aiguilles Rouges (Barfety *et al.*, 2000; Von Raumer and Bussy, 2004). Inspection of screes in multiple areas indicates that these serpentinites are ubiquitous in the metamorphic basement of the Pelvoux Massif, although in very subordinate volume (Fig. 2). When observed in place, they mostly occur as meter to decameter-wide lenses, which can be up to a hundred meters long. Some of them are concordant with the surrounding metamorphic foliation, but they are commonly transposed in brittle fault zones, as they acted as a weak layer localizing deformation (Fig. 3e). Thus, most of these serpentinites have been strongly deformed and retrogressed, and do not preserve any relics of olivine, pyroxene or any other primary mineral that existed before serpentinization. A second type of peculiar ultramafic rocks was reported by Le Fort (1971) and Pecher (1970) as "amphibolite boulders with a concentric structure". They occur as decimeter-size dark boulders in migmatites, and consist of a core composed of amphiboles (actinolite-tremolite, hornblende, anthophyllite), chlorite, iron oxides, phlogopite, calcite, and a few relics of spinel and augite, which is surrounded by centimeter-wide reaction coronas of tremolite and biotite. The rocks described by Le Fort (1971) were obviously heavily retrogressed and did not preserve much of their initial assemblages. Thus, their origin remained unclear. They were regarded either as relics of metasomatized calc-silicate boudins, or as ultramafic cumulates of gabbro-dolerite series similar to the Chamrousse ophiolite in the massif of Belledonne.
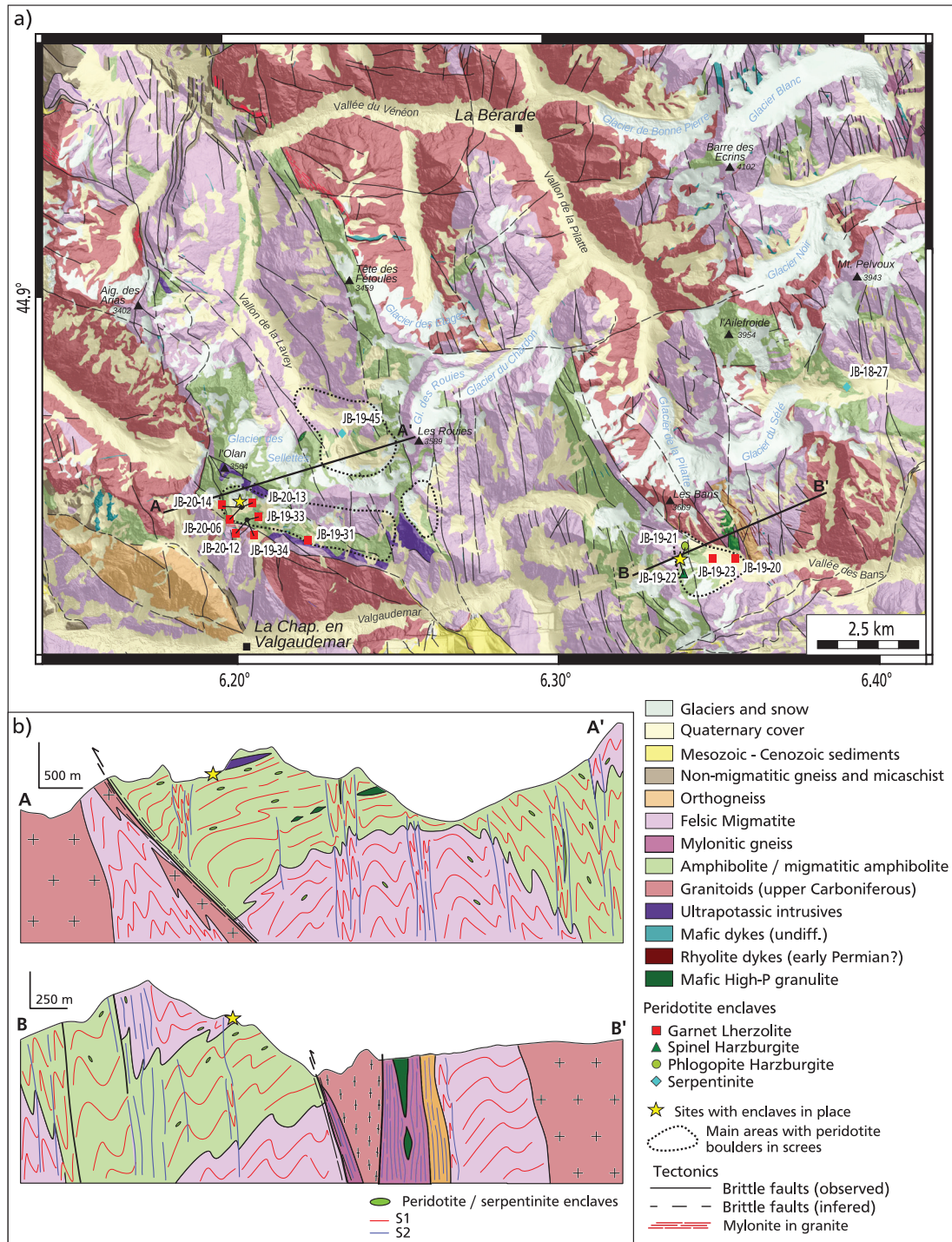
Fig. 2. (a) Geological map of Central Pelvoux, modified from the BRGM 1:50 000 map of Saint-Christophe en Oisans (Barféty and Pêcher, 1984) with the position and nature of collected samples. Two sites were peridotites have been observed in place are shown with yellow stars. Areas were peridotite enclaves are relatively abundant in screes are highlighted by black dotted lines. (b) Interpretative cross-sections in the Olan-Rouies and Bans areas showing the general structuration of the massif, after Jacob *et al.* (2022) and Fréville *et al.* (2022). Ultramafic enclaves are found both in the flat-lying S1 and in the subvertical S2.

Fig. 2. (a) Carte géologique de la partie centrale du massif du Pelvoux, modifiée à partir de la feuille BRGM 1:50 000 de Saint-Christophe en Oisans (Barféty et Pêcher, 1984), avec la position et la nature des échantillons collectés. Deux sites où des péridotites peuvent être observées en place sont indiqués par des étoiles jaunes. Les zones où les enclaves de péridotites sont relativement abondantes dans les éboulis sont mises en évidence par des lignes pointillées noires. (b) Coupes géologiques interprétatives montrant la structure générale du massif, d'après Jacob et al. *(2022) et Fréville* et al. *(2022). Les enclaves ultramafiques se trouvent à la fois dans les foliations S1 et S2.*
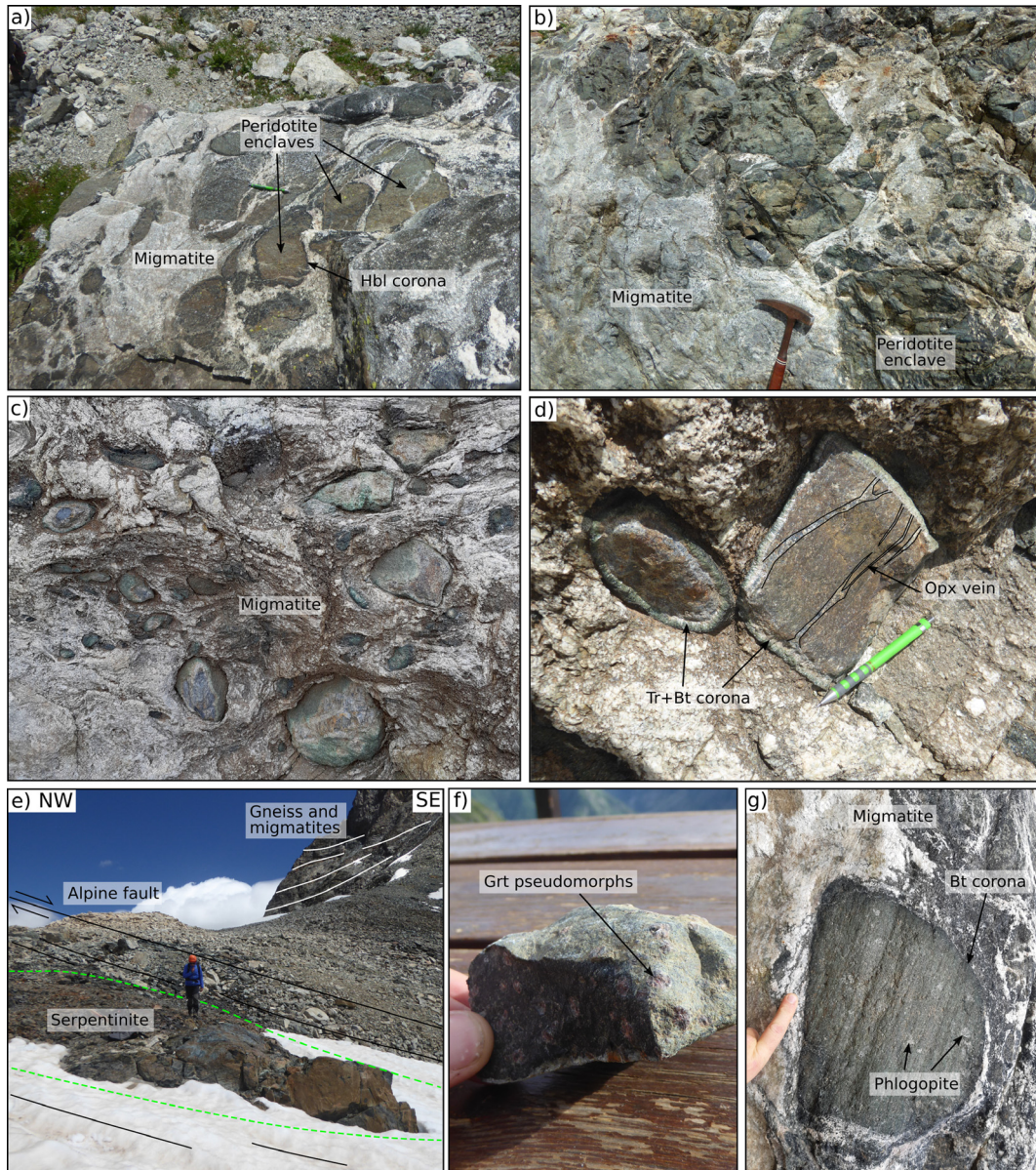
Fig. 3. Field pictures of peridotite and serpentinite outcrops in the Pelvoux Massif. (a) Decameter-wide boulder of diatexitic migmatite containing multiple enclaves of peridotite and amphibolite, eastern side of Sellar Pass (N44.8344°; E06.3440°). Enclaves are surrounded by a thin hornblende-bearing coronas at the contact with migmatite. (b) Same kind of peridotite enclaves in diatexitic migmatite on the southern slopes of Olan, Valgaudemar (N44.8509°; E06.2031°). Reaction with the migmatite is very limited here, and enclaves display sharp border devoid of wide coronas. (c, d) Peridotite enclaves in place in a diatexitic migmatite, eastern side of Sellar pass (N44.8361°; E06.3391°). Enclaves display 1–3 cm-wide coronas composed of radially-oriented tremolite surrounded by a second rim of biotite, and are cut by centimeter-wide veins of orthopyroxenite. (e) Serpentinite outcrop at the Sellettes pass. The serpentinites are transposed in an alpine brittle fault oblique to the Variscan foliation (N44.8540°; 06.2181°). (f) Hand-size sample of retrogressed garnet lherzolite (JB-19-33) found in a scree above the Olan hut (see Tab. 1 for coordinates). (g) Close-up view of a phlogopite-bearing peridotite enclave on the large block of picture (a).

Fig. 3. Photos des principaux affleurements de péridotite et de serpentinite dans le massif du Pelvoux. (a) Bloc décamétrique dans des migmatite (diatexite), contenant de multiples enclaves de péridotite et d'amphibolite; versant est du col du Sellar (N44,8344° ; E06,3440°). Une fine couronne de hornblende entoure les enclaves au contact de la migmatite. (b) Même type d'enclaves de péridotite dans une migmatite diatexitique sur les pentes sud de l'Olan, Valgaudemar (N44,8509° ; E06,2031°). La réaction avec la migmatite est ici très limitée, et les enclaves présentent par endroits une bordure nette dépourvue couronnes réactionnelles. (c, d) Enclaves de péridotite en place dans une migmatite diatexitique, côté est du col de Sellar (N44,8361° ; E06,3391°). Les enclaves présentent des couronnes réactionnelles de 1 à 3 cm de large, composées de trémolite se développant de façon radiaire, elles-mêmes entourée d'une seconde couronne de biotite. Le coeur des enclaves est recoupé par des veines d'orthopyroxénite de largeur centimétrique. (e) Affleurement de serpentinite au niveau du col des Sellettes. Ces serpentinites sont transposées dans une faille cassante alpine, qui recoupe la foliation varisque (N44,8540° ; 06,2181°). (f) Échantillon de lherzolite à grenat rétromorphosée (JB-19-33) trouvé en éboulis au-dessus du refuge d'Olan (coordonnées en Tab. 1). (g) Gros plan sur une enclave de péridotite à phlogopite sur le gros bloc de la photo (a).

Table 1. List of collected samples with name, localization (WGS84), petrographic type and bulk composition in major elements recalculated on an anhydrous basis and normalized to 100 wt%. < d.l: values below detection limit. Grt Lrz: Garnet Lherzolite; Spl Hrz: Spinel Harzburgite; Phl Hrz: Phlogopite–chromite Harzburgite; Srp: Serpentinite.

Tableau 1. Liste des échantillons collectés avec nom, localisation (WGS84), type pétrographique et composition roche totale éléments majeurs, recalculée sur une base anhydre et normalisée à 100 % (en masse). < d.l : valeurs inférieures à la limite de détection. Grt Lrz : Lherzolite à grenat ; Spl Hrz : Harzburgite à spinelle ; Phl Hrz : Harzburgite à phlogopite–chromite ; Srp : Serpentinite.

Sample		Position (WGS84)		wt% oxides											
Name	Type	Long°	Lat°	SiO_2	TiO_2	Al_2O_3	FeO	MnO	MgO	CaO	Na_2O	K2O	P_2O_5	Mg#	Cr#
JB-19-20	Grt Lrz	6.35604	44.83521	45.11	0.11	3.29	8.14	0.12	40.70	2.33	0.20	< d.l	< d.l	0.90	0.07
JB-19-23	Grt Lrz	6.34905	44.83562	48.19	0.06	2.20	8.67	0.12	39.16	1.41	0.14	0.05	< d.l	0.89	0.11
JB-19-31	Grt Lrz	6.22290	44.84258	46.52	0.15	3.72	8.15	0.10	38.11	2.69	0.26	0.29	< d.l	0.89	0.06
JB-19-33	Grt Lrz	6.20450	44.84665	45.33	0.15	3.62	8.52	0.11	39.46	2.58	0.23	< d.l	< d.l	0.89	0.06
JB-19-34	Grt Lrz	6.20450	44.84665	45.71	0.13	3.41	8.29	0.08	40.23	2.02	0.13	< d.l	< d.l	0.90	0.07
JB-20-06	Grt Lrz	6.20309	44.84967	46.06	0.11	2.78	8.30	0.08	40.54	1.93	0.16	0.04	< d.l	0.90	0.08
JB-20-12	Grt Lrz	6.20473	44.84611	45.98	0.15	3.80	8.33	0.08	38.71	2.65	0.27	0.04	< d.l	0.89	0.07
JB-20-13	Grt Lrz	6.20319	44.84945	45.22	0.17	4.49	8.29	0.11	38.60	2.84	0.22	0.06	< d.l	0.89	0.06
JB-20-14	Grt Lrz	6.20274	44.84982	45.72	0.05	2.20	8.09	0.11	41.98	1.62	0.08	0.15	< d.l	0.90	0.11
JB-19-21	Phl Hrz	6.33910	44.83612	45.98	0.10	1.03	8.45	0.10	43.21	0.36	< d.l	0.64	0.13	0.90	0.35
JB-19-22	Spl.Hrz	6.33910	44.83612	44.69	0.03	1.63	8.79	0.10	42.94	1.42	0.08	0.33	< d.l	0.90	0.14
JB-18-27	Srp	6.39256	44.87250	45.01	< d.l	1.22	9.11	0.11	44.15	0.39	< d.l	< d.l	< d.l	0.90	0.20
JB-19-45	Srp	6.23450	44.86690	46.66	< d.l	1.26	8.17	0.08	42.75	0.79	< d.l	0.29	< d.l	0.90	0.18
JB-19-48	Srp	6.10814	45.23891	46.20	0.04	1.59	8.98	0.07	42.86	0.28	< d.l	< d.l	< d.l	0.89	0.15
JB-19-49	Srp	6.11245	45.23940	46.20	< d.l	0.84	8.84	0.05	43.63	0.43	< d.l	< d.l	< d.l	0.90	0.24

Extensive investigation of the screes in the area covered by the map in Figure 2 has led us to find well-preserved specimens of these boulders, with limited reactions with the migmatites, which contain a primary assemblages dominated by olivine, orthopyroxene and clinopyroxene, with spinel and/or garnet. It is therefore clear that these rocks are retrogressed peridotites. The main occurrences have been found in screes on the southern slopes of Valgaudemar Valley, between the summits of Olan and Les Rouies, and in the Bans Valley. Two sites where they are in place are shown with yellow stars in Figure 2. The first one is located on the eastern side of the Sellar pass, in the Bans Valley (GPS: N44.83612°, E6.33910°, alt. 2770 m), and the second one above Refuge de l'Olan (GPS: N44.85089°, E6.20314°, alt. 2744 m). These peridotites form rounded to sub-angular 5 cm to 1 m wide enclaves. They generally occur in highly-mobilized part of migmatites (diatexites), and commonly appear as "nest" of enclaves, without any particular orientation (Figs. 3a–3c). This disposition suggests the enclaves represent pieces of larger peridotite bodies, possibly up to decameter-size, which have been fractured during injection of granitic magmas and dismembered into smaller blocks. The enclaves are neither particularly elongated (aspect ratios between 1 and 1.8) nor oriented in any preferential direction, which suggests they did not experience significant ductile deformation in the migmatite. Reaction with the hosting migmatite is evidenced by the development of coronas around the peridotite enclaves. However, they are not systematic. Some enclaves are almost devoid of these coronas, and display instead sharp contacts with the migmatite (Fig. 3b), while hornblende ± biotite reaction coronas may develop in other cases (Figs. 3a and 3c). The most spectacular ones have been observed on peridotites from the Sellar pass, and consist of a 1–3 cm wide coronas of radially-oriented tremolite, surrounded by a ca. 0.5–1 cm concentric layer of biotite (Figs. 3c and 3d). However, these coronitic reactions only affected the enclaves at their outer rims or along fracturation pathways, leaving the inner parts of largest enclaves (> 10 cm) relatively well-preserved (Figs. 3f and 3g).

3 Samples and methods

Eleven samples of peridotite and 4 samples of serpentinite were collected for petrological study and whole-rock geochemical and isotopic analyses. All the samples come from the Pelvoux Massif, excepted two samples of serpentinite collected in a large hectometer-size lense in the Belledonne Massif. Sampling coordinates and petrological classification of each sample are summarized in Table 1.

3.1 Petrography and mineral analysis

Backscattered electron (BSE) images were acquired at ISTerre Grenoble with a Tescan Vega 3 scanning electron microscope equipped with an energy dispersive spectrometer (EDS) for semi-quantitative analysis. It was operated with an accelerating voltage of 16 kV and a beam current of 10 nA. Inclusions in garnet were identified by Raman spectroscopy, using a Horiba Labram Soleil instrument installed at ISTerre Grenoble, with a 532 nm laser beam. Mineral compositions were measured using a JEOL JXA-8230 electron probe microanalyzer (EPMA) at ISTerre Grenoble, which is equipped with five wavelength dispersive spectrometers (WDS) and an additional EDS. All silicates except olivine

were analyzed using standard EPMA protocols, with an accelerating voltage of 15 kV (amphibole, phlogopite) to 20 kV (garnet, pyroxenes), a beam current of 10 nA (amphibole, phlogopite) to 20 nA (garnet, pyroxenes), and a counting time per element of 30 to 60 s for peak and both background positions. Natural minerals and synthetic glass were used for standardization, and the ZAF matrix procedure was applied for data reduction. The spot size was set to 1–3 µm depending on the size of minerals and the presence of volatile elements.

The composition of olivine was analyzed following high-precision method for major (Si, Mg, Fe), minor (Ni, Mn) and trace (Al, Ca, Cr, Ti, P) elements (Batanova *et al.*, 2015) at an acceleration voltage of 20 kV, beam current of 900 nA and beam diameter of 2 microns. Total analysis time of each point was 7.2 minutes. MongOl sh11-2 olivine reference material (Batanova *et al.*, 2019) was used as primary standard to verify precision and accuracy (*e.g.* Sobolev *et al.*, 2007). Deviation from the reference measured during the analytical session was between 2 and 13 ppm for trace elements, between 10 and 85 ppm for minor elements and between 0.01 and 0.06 wt% for major oxides, which is in any cases below the 2-sigma uncertainty reported in Batanova *et al.* (2019). The composition of Cr-spinel was measured at 20 kV and 50 nA beam current. Counting time was adapted to element content and was between 60 to 120 s for each element (for peak and both background positions). The standardization was made using a synthetic oxide standard set (P&H Developments Ltd., Calibration Standards for Electron Probe Microanalysis, Standard Block GEO) for all elements except Mn (on rhodonite). Ferric iron in spinel was calculated assuming perfect stoichiometry. Repeated measurements of the chromite USNM 117075 (Jarosewich *et al.*, 1980) standard and spinel samples Bar 8601-10 and Dar 8502-2, whose Fe^{3+}/Fe_{total} ratio had been measured by Mossbauer spectroscopy (Ionov and Wood, 1992) have shown that the selected method provides Fe^{3+}/Fe_{total} ratios accurate to within the measurement error. Spinel Bar 8601-10 (Ionov and Wood, 1992) was used as a primary standard and was analyzed multiple times during the session to verify precision and accuracy. Deviation from the reference value measured during the session was below 50 ppm for most of trace elements (Ti, V, Mn, Ni) and bit higher for Zn (66 ppm) and Si (86 ppm). For major oxides, deviation from the reference value was about 0.64 wt% for Al_2O_3 and 0.06 wt% for FeO and MgO.

3.2 Whole-rock composition

Samples were cut to remove the coronas formed at the contact with the migmatites, and domains devoid of large veins were carefully selected to study only the best-preserved domains. They were then crushed in a jaw crusher and pulverized into a 70–80 µm powder using an agate crusher.

whole-rock geochemical analyses were performed at the SARM in Nancy, using a Thermo Fischer iCap6500 ICP-OES for major oxides and an iCapQ ICP-MS for minor and trace elements. Details about the analytical procedures for whole-rock geochemical analyses are described in Carignan *et al.* (2001). Samples display high loss on ignition between 7 and 13% due to serpentinization, and therefore the analyses were recalculated on an anhydrous basis to allow comparison

between samples. Raw analyses are provided in the Supplementary Material. The R-based GCDKit software (Janoušek *et al.*, 2016) was used for statistical analysis and plotting of whole-rock geochemical data.

3.3 Sr–Nd isotopes

Nine samples were selected for Sr–Nd isotope analyses. Due to low Nd concentration, only five of them were analyzed for Nd isotopes. Isotopic measurements were also carried out at the SARM in Nancy. 100 to 200 mg of powdered samples were dissolved into a mixture of concentrated HNO_3 and HF heated to 115 °C during 24 to 48 h, followed by concentrated HCl at 125 °C during 24 h.

Sr and Nd were isolated *via* ion-exchange chromatography using Sr.Spec, Tru.Spec and Ln.Spec resins, following the procedure described in Pin *et al.* (1994) and Pin and Zalduegui (1997). Sr and Nd isotopes were analyzed by thermal ionization mass spectrometry (TIMS), using respectively a Triton Plus and a Neptune Plus instrument operated in static multi-collection mode. The $^{87}Sr/^{86}Sr$ ratios were corrected for mass bias assuming $^{87}Sr/^{88}Sr = 0.119400$, and $^{143}Nd/^{144}Nd$ ratios were corrected to $^{146}Nd/^{144}Nd = 0.721900$ (Luais *et al.*, 1997). Internal standards NBS 987 and JNdi-1 (Tanaka *et al.*, 2000) were used for Sr and Nd, respectively. The decay constants applied to age-correct the isotopic ratios are from Steiger and Jäger (1977) for Sr and Lugmair and Marti (1978) for Nd. The εNd_i values were obtained using composition of the chondritic uniform reservoir (CHUR) of Bouvier *et al.* (2008).
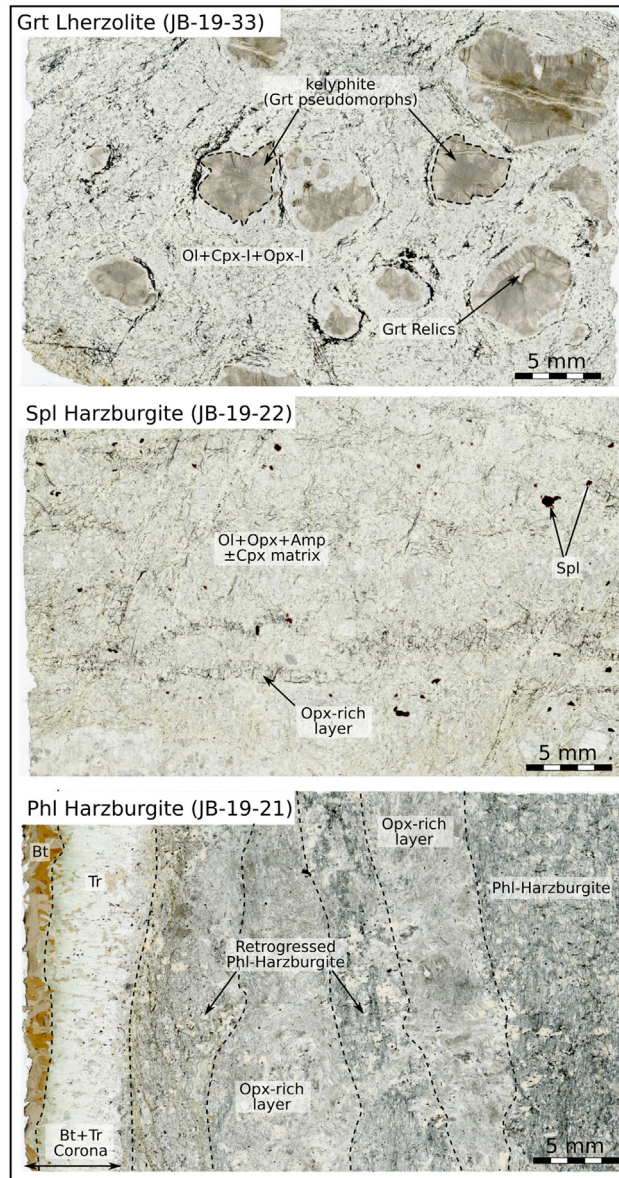
4 Petrography

All the samples collected in the ultramafic enclaves have been retrogressed to various degrees and contain a high amount of volatiles (loss on ignition between 7 and 13 wt%), which reflects fluid addition during retrogression. Typical serpentinization textures are observed, with the development of a mesh of serpentine + Fe-oxide in cracks and at olivine grain boundaries. Minor amount of carbonates are also observed in the most retrogressed samples. Four different types of ultramafic rocks have been identified based on petrological observations: serpentinites (4 samples), retrogressed garnet lherzolite (9 samples), retrogressed spinel harzburgite (1 sample) and retrogressed phlogopite-chromite harzburgite (1 sample; Fig. 4). The serpentinites present whole-rock major element compositions similar to the harzburgites (see Sect. 6, Geochemistry Section below), but rarely preserve relics of their primary minerals. They are mostly composed of HT serpentine (antigorite) and Fe-oxides, with a few relics of spinel. Petrological descriptions are therefore focused on the peridotite samples.

4.1 The garnet lherzolites

The garnet lherzolites are the most distinctive type in the field. Macroscopically, they are composed of a dark green, fine-grained matrix containing millimeter to centimeter-size reddish spots (former garnet) and millimeter-size grains of
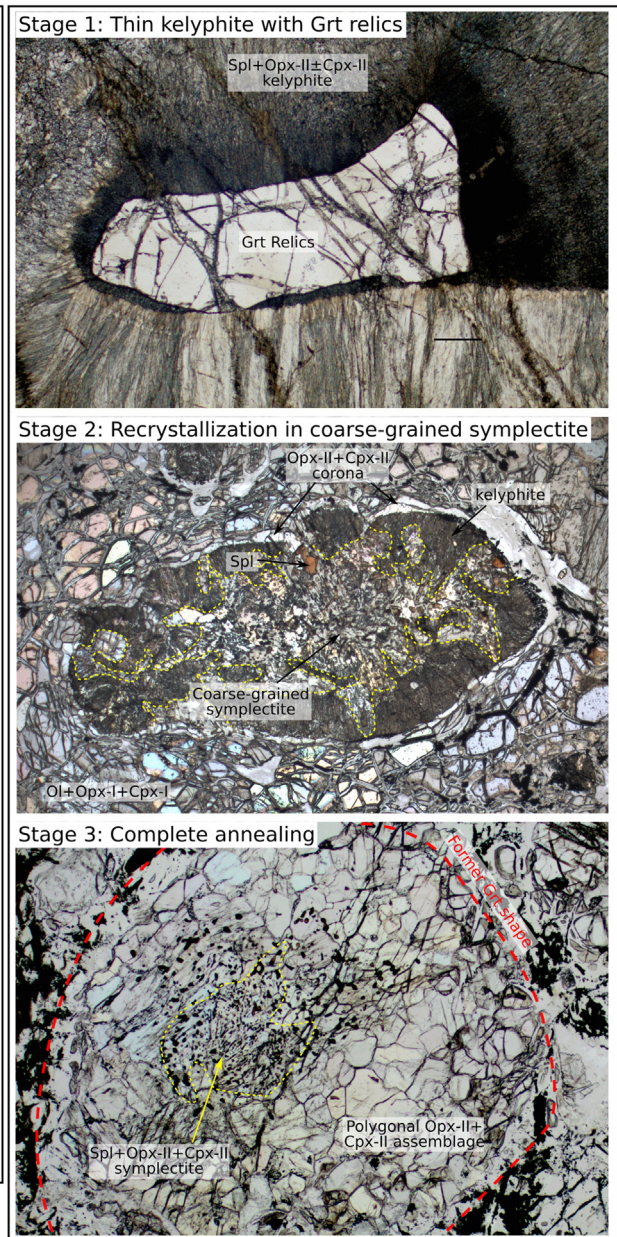
Fig. 4. (a) Thin section scans of representative samples from the three petrographic groups identified in the field (garnet lherzolites, spinel harzburgites, phlogopite-chromite harzburgites). Note the presence of Opx-rich layers in the harzburgites, which may be related to melt-rock interaction. (b) Polarizing microscope images showing the successive stages of recrystallization in the kelyphite formed by destabilization of garnet. Stage 1: Thin kelyphite composed of micrometer-scale intergrowth of spinel + enstatite ± diopside, containing a few relics of garnet. Stage 2: Recrystallization into a coarser-grained symplectite of spinel + enstatite ± diopside. Amphibole may occur in some samples, due to external fluid input during garnet recrystallization. Stage 3: complete annealing of the symplectites, which have recrystallized into a polygonal assemblage of enstatite + diopside, with relics of spinel.

Fig. 4. *(a) Scans de lames minces d'échantillons représentatifs des trois groupes pétrographiques identifiés sur le terrain (lherzolites à grenat, harzburgites à spinelle, harzburgites à phlogopite-chromite). Notez la présence de niveaux riches en Opx dans les harzburgites, qui semblent résulter d'interactions avec un magma silicaté. (b) Images prises au microscope polarisant, montrant les étapes successives de recristallisation des kelyphites formées par la déstabilisation du grenat. Stade 1 : kelyphites fines, composée d'intercroissance à l'échelle micrométrique de spinelle + enstatite ± diopside, contenant quelques reliques de grenat. Stade 2 : Recristallisation en symplectites plus grossières à spinelle + enstatite ± diopside. De l'amphibole peut être présente dans certains échantillons, en raison d'un apport extérieur de fluide pendant la recristallisation du grenat. Stade 3 : texture de recuit des symplectites, qui ont recristallisé en un assemblage polygonal à enstatite + diopside, avec quelques reliques de spinelle.*

diopside (Figs. 3f and 4a). The dark matrix contains 100–200 μm grains of enstatite (labeled Opx-I in Fig. 5a), diopside (Cpx-I) and olivine (Fig. 5a). Garnet is almost completely destabilized, and only a few millimeter-size relics were identified (Fig. 4). Most of the former grains (reddish spots) have been replaced by kelyphites mainly composed of micrometer-size intergrowth of spinel and enstatite (Opx-II in Fig. 5b) with subordinate amounts of larger grains (10–20 μm) of diopside (Cpx-II) and amphibole. These kelyphites are surrounded by a coarse-grained corona of enstatite (Opx-II) + diopside (Cpx-II) (Figs. 5a and 5c). In most samples, the fine-grained kelyphite has partially recrystallized into a coarse-grained globular symplectite of orthopyroxene + spinel ± clinopyroxene ± amphibole and eventually evolved toward a coarse-grained polygonal assemblage of the same minerals with relics of vermicular spinel (Figs. 4b and 5c). The rare garnet relics are directly surrounded by a second generation of symplectite composed of plagioclase + amphibole + Cr-rich spinel (Fig. 5b). The garnet relics contain small inclusions (ca. 20 μm wide) of orthopyroxene, which themselves contain tiny dark inclusions of graphite, identified by Raman spectroscopy (Fig. 5d).

4.2 The spinel-pargasite-(phlogopite) harzburgite (JB-19-22)

The harzburgite sample JB-19-22 is mostly composed of olivine, enstatite, pargasitic amphibole and Mg-spinel, with rare diopside, phlogopite, and accessory Fe-oxides (Figs. 4a, 6a and 6b). Spinel forms 200–500 μm grains that contain inclusions of pargasitic amphibole (Fig. 6b), but never occurs in symplectites or kelyphites like in the garnet lherzolites, which suggests that garnet was absent from the primary assemblage. Olivine forms 50–200 μm grains, which have been partly serpentinized (Fig. 6a). Enstatite is abundant and forms large grains up to 500 μm wide. The largest grains are preferentially localized in discontinuous, millimeter-wide bands (Fig. 4a). By contrast, diopside is extremely rare and only a few grains < 100 μm, rimmed by amphibole, were identified (Fig. 6c). Pargasite forms 100–300 μm grains and occurs as smaller inclusions in spinel. Phlogopite is scarce and generally found in association with pargasite.

4.3 The phlogopite-chromite harzburgite (JB-19-21)

The phlogopite-chromite harzburgite contains olivine, enstatite, phlogopite, chromian spinel (chromite) and accessory apatite, and is completely devoid of clinopyroxene (Figs. 4a and 6d). The sample investigated in detail (JB-19-21) is an enclave surrounded by a thick corona of biotite and tremolite (Figs. 3c, 3d and 4a), but large grains of phlogopite are also visible in some enclaves devoid of large reaction coronas (Fig. 3g). Olivine forms partly serpentinized grains 200–500 μm in size (Fig. 5d). Enstatite and phlogopite form large grains up to 1 mm-wide. Chromite is ubiquitous. It forms subeuhedral grains ranging from 10 μm to > 100 μm, which occur either in the serpentinized matrix or as inclusions in phlogopite, and contain itself small inclusions of phlogopite (Fig. 6e). Apatite is also closely associated with phlogopite, and generally occurs

in contact with this mineral (Fig. 6d). Harzburgitic domains are cut by centimeter-wide sub-parallel veins of orthopyroxenite (Fig. 3a), which are mainly composed of large grains of enstatite (up to 3 mm wide), with subordinate olivine, phlogopite and chromite (Fig. 6f). Partial replacement of Mg-rich primary olivine by, BSE-brighter Fe-rich secondary olivine is commonly observed in olivine grains located close to or within these orthopyroxenite veins (Fig. 6f). This replacement has mostly occurred in the rims and along cracks, leaving the olivine cores unmodified (Fig. 6f).

5 Mineral composition

Mineral composition has been investigated by EPMA in three samples: a garnet lherzolite (JB-19-33), a spinel-pargasite-(phlogopite) harzburgite (JB-19-22) and a phlogopite-chromite harzburgite (JB-19-21). A set of selected representative analyses is provided in Tables 2 and 3. The complete set of electron microprobe analyses is provided in the Supplementary Material.

In all samples, olivine displays high Mg# (molar ratio $Mg/Mg + Fe^{2+}$) between 0.88 and 0.91, high Ni (2700–4200 ppm) and moderate Mn (1000–1300 ppm) content, with Ni/Mn between 2.1 and 3.3 (Fig. 7a), which is indicative of mantle peridotite olivine and precludes any cumulative origin for these samples (Wang *et al.*, 2021). This is consistent with the low concentrations in trace elements: below 50 ppm for Ti and Al and below 200 ppm for Ca, Cr and P. In sample JB-19-21 (phlogopite-chromite bearing harzburgite), the rims of olivine grains within or close to the orthopyroxenite layers have lower Mg# (0.81–0.86) and higher Mn content (Mn = 2000–5800 ppm) than the cores, with low Ni/Mn between 0.32 and 1.74. This suggests this olivine population formed by reaction between mantle olivine and melts. Composition variations are observed between samples. In particular, there is a consistent increase in Ni/Mn correlated with increasing Mg# (Fig. 7a), from the least magnesian olivine in clinopyroxene-garnet lherzolites (Ni/Mn = 2.1–2.3) to the more magnesian olivine in clinopyroxene-free phlogopite-chromite harzburgite (Ni/Mn = 3.0–3.3).

Enstatite displays high Mg# between 0.89 and 0.91. As for olivine, enstatite displays an increase in Mg# correlated with decreasing Mn content from the garnet lherzolite to the phlogopite-chromite harzburgite (Fig. 7b). Al content of enstatite is very low in the phlogopite-chromite harzburgite (ca. 0.01 p.f.u) and higher in the spinel harzurgite (0.09–0.13 p.f.u) and the garnet lherzolite (Opx-I: 0.05–0.08 p.f.u). In the latter sample, secondary enstatite that crystallized in the coronas aroud garnet (Opx-II) displays higher Al-content up to 0.15 p.f.u, but does not show significant difference in Mg# with Opx-I (Fig. 7c).

Diopside and garnet were analyzed only in the garnet lherzolite. Diopside has high Mg# (0.92–0.94 p.f.u) and variable Al (0.14–0.17 p.f.u Al). Diopside in the coronas (Cpx-II) contains slightly more Al and slightly less Cr than primary diopside Cpx-I, with again no difference in Mg# (Fig. 7d).

Garnet is a slightly chromian pyrope (Cr# = 0.04–0.05). Composition profile (Fig. 7e) reveals a slight Mg-decrease and Fe-increase from core to rim (from $Prp_{73}Alm_{15}Grs_{11}$ to $Prp_{65}Alm_{23}Grs_{11}$)
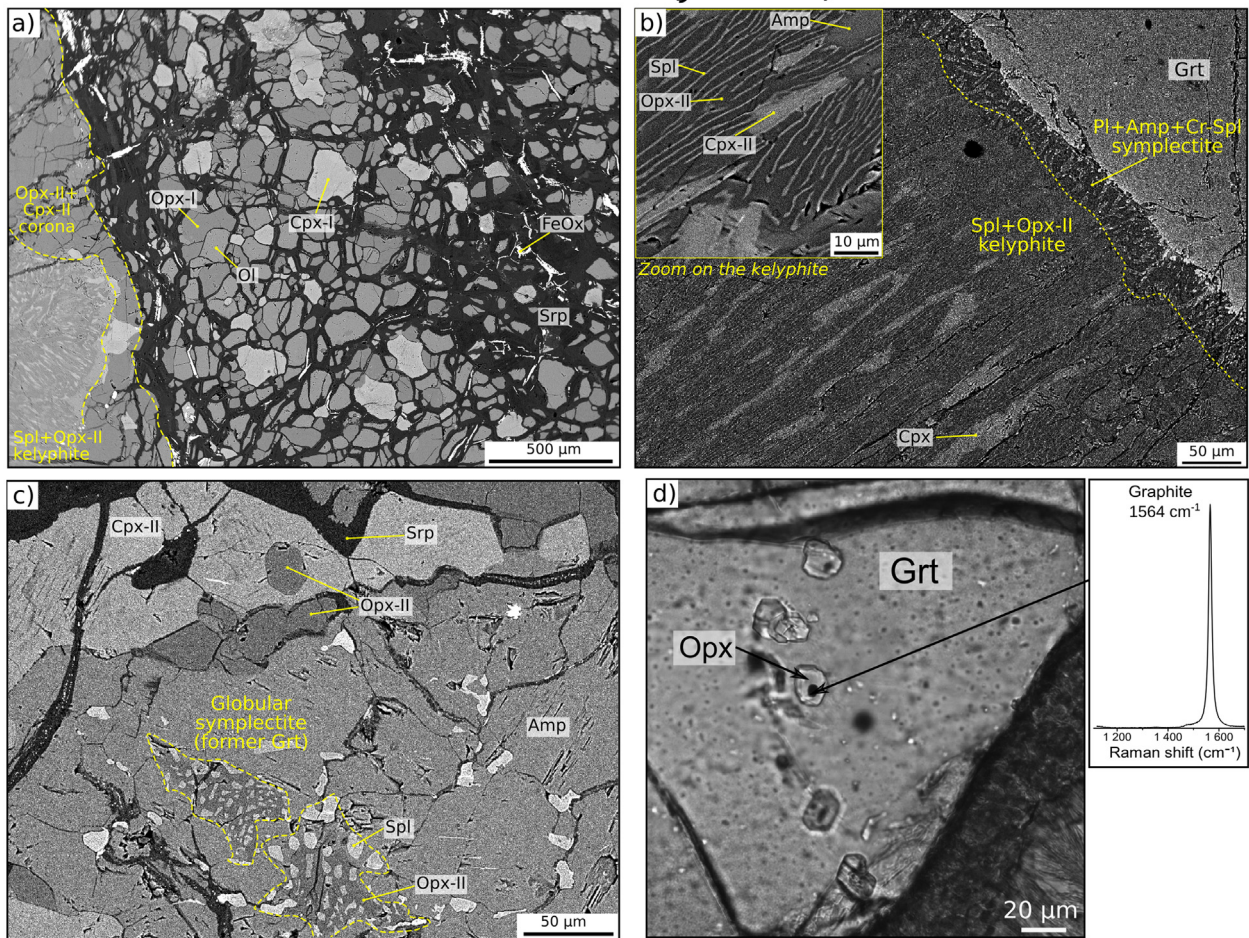
Grt Lherzolite (JB-19-33)

Fig. 5. Backscatterred electron (BSE) and optical microscope images of the garnet lherzolites (sample JB-19-33). (a) BSE wide view on the lherzolite matrix, with a former grain of garnet on the bottom left. Note the abundance of diopside (Cpx-I) in the matrix, typical of a lherzolite. Garnet has been replaced by a kelyphite surrounded by a coarse-grained corona of clinopyroxene + orthopyroxene (Cpx-II + Opx-II). (b) Zoom on an Opx + Spl ± Cpx kelyphite surrounding a relic of garnet (top-right). A thin 20–50 μm-wide symplectite of amphibole + plagioclase ± Cr-spinel has developed at the contact with the garnet relics during a later stage of retrogression. (c) Advanced stage of annealing of a former kelyphite, which has been replaced by a coarse-grained assemblage of amphibole, orthopyroxene, clinopyroxene and Cr-spinel. Relics of a globular spinel + orthopyroxene symplectite is visible in the centre. (d) Close-up view on orthopyroxene inclusions in a garnet relics of sample JB-19-33 (reflected light optical microscopy). Raman spectroscopy on the tiny dark inclusions in orthopyroxene reveals the presence of graphite, indicated by a strong peak around 1566–1575 cm^{-1} (Beyssac *et al.*, 2002).

Fig. 5. Images en microscopie électronique (électrons rétrodiffusés, BSE) et en microscopie optique (lumière réfléchie) d'une lherzolites à grenat (échantillon JB-19-33). (a) Image en BSE de la matrice de la lherzolite, avec un ancien grain de grenat en bas à gauche. Notez l'abondance du diopside (Cpx-I) dans la matrice, typique d'une lherzolite. Le grenat a été remplacé par une kelyphite, entourée d'une couronne à gros grains de clinopyroxène + orthopyroxène (Cpx-II + Opx-II). (b) Zoom sur une kelyphite à Opx + Spl ± Cpx entourant une relique de grenat (en haut à droite). Une fine symplectite de 20–50 μm de large à amphibole + plagioclase ± spinelle chromifère s'est développée au contact des reliques de grenat pendant un stade ultérieur de rétromorphose. (c) Stade avancé de recristallisation d'une ancienne kelyphite, qui a été remplacée par un assemblage à gros grains d'amphibole, d'orthopyroxène, de clinopyroxène et de spinelle chromifère. Les restes d'une symplectite globulaire à spinelle + orthopyroxène sont visibles au centre. (d) Gros plan sur des inclusions d'orthopyroxène dans les reliques de grenat de l'échantillon JB-19-33 (microscopie optique en lumière réfléchie). Les spectres Raman obtenus sur les petites inclusions sombres dans les orthopyroxènes révèle la présence de graphite, indiquée par un pic à environ 1566–1575 cm^{-1} (Beyssac et al., 2002).
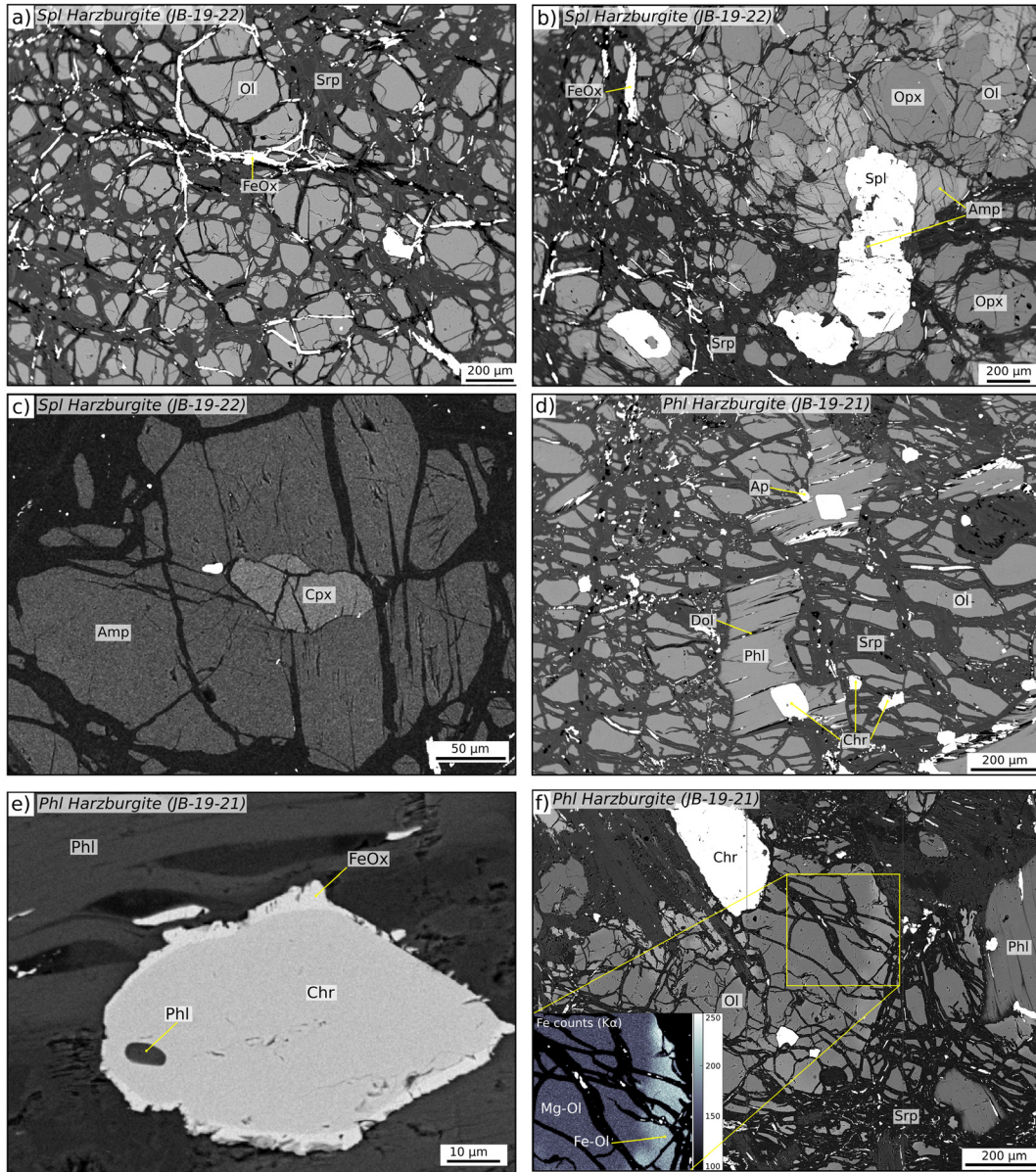
Harzburgites (JB-19-21; JB-19-22)

Fig. 6. Backscatterred electron (BSE) images of harzburgites (samples JB-19-21 and JB-19-22). (a) Olivine-dominated assemblage in sample JB-19-22 (Spinel harzburgite), which is almost devoid of clinopyroxene. (b) Large grain of spinel in the spinel harzburgite (JB-19-22). This sample is rich in pargasite, which occurs as 100–200 μm grains and as inclusions in spinel. (c) Rare grain of clinopyroxene surrounded by pargasite in the spinel harzburgite. (d) Mineral assemblage in the phlogopite-chromite harzburgite (JB-19-21). Chromite is ubiquitous and can be found as inclusion in phlogopite. Apatite and dolomite commonly crystallize close to phlogopite. (e) Close-up view on a grain of chromite, which contains a 5-μm wide inclusion of phlogopite. (f) Zoned olivine close to an orthopyroxenite layer, with a Mg-rich core surrounded by a BSE-brighter rim of Fe–Mn-rich olivine. Fe X-ray mapping reveals an irregular boundary between Mg-rich and Fe-rich domains. Note that this zoning is cut by the serpentine network, which indicates that partial replacement of Mg-rich by Fe–Mn-rich olivine predates serpentinization.

Fig. 6. *Images en microscopie électronique (BSE) des harzburgites (échantillons JB-19-21 et JB-19-22). (a) Assemblage dominé par l'olivine dans l'échantillon JB-19-22 (harzburgite à spinelle), qui est presque dépourvu de clinopyroxène. (b) Gros grain de spinelle dans la harzburgite à spinelle (JB-19-22). Cet échantillon est riche en pargasite, qui se présente sous forme de grains de 100–200 μm et d'inclusions dans les spinelles. (c) Rare grain de clinopyroxène entouré de pargasite dans la harzburgite à spinelle. (d) Assemblage minéral dans la harzburgite à phlogopite-chromite (JB-19-21). La chromite est omniprésente et peut se présenter sous forme d'inclusion dans la phlogopite. L'apatite et la dolomite cristallisent à proximité de la phlogopite. (e) Zoom sur un grain de chromite, qui contient une inclusion de phlogopite de 5 μm de large. (f) Olivine zonée près d'un niveau d'orthopyroxénite, avec un coeur riche en Mg entouré d'une bordure plus claire riche en Fe et Mn. La cartographie du Fe révèle une limite irrégulière entre les domaines riches en Mg et en Fe. On peut noter que la zonation est recoupée par des veines de serpentine, ce qui indique que le remplacement de l'olivine riche en Mg par l'olivine riche en Fe–Mn est antérieur à la serpentinisation.*

Table 2. Representative electron microprobe analyses of garnet, orthopyroxene, clinopyroxene, amphibole and phlogopite. na: not analyzed. The complete set of analyzes with end-member recalculations is provided in the Supplementary Material.

Tableau 2. *Sélection représentative d'analyses à la microsonde électronique du grenat, de l'orthopyroxène, du clinopyroxène, de l'amphibole et de la phlogopite. na : non analysé. Le jeu de données complet est disponible en matériel supplémentaire.*

Sample	JB-19-33	JB-19-33	JB-19-21	JB-19-22	JB-19-33	JB-19-33	JB-19-33	JB-19-33	JB-19-21	JB-19-22	JB-19-21	JB-19-21
Mineral	*Grt*	*Grt*	*Opx*	*Opx*	*Opx*	*Opx*	*Cpx*	*Cpx*	*Amp*	*Amp*	*Phl*	*Bt*
LABEL	*Grt-12*	*Grt-01*	*Opx-02*	*Opx-04*	*Opx-07*	*Opx-08*	*Cpx-11*	*Cpx-06*	*Amp-5*	*Amp-1*	*Phl-04*	*Phl-11*
Position	core	rim	core	core	Matrix Core	Grt Corona	Grt Corona	*Matrix Core*	Corona	core	core	Corona
wt% oxides												
SiO_2	41.32	41.45	57.57	56.02	55.71	55.01	52.99	53.49	55.29	44.74	41.27	38.32
TiO_2	0.63	0.61	0.06	0.03	0.09	0.07	0.34	0.31	0.03	0.39	1.15	2.02
Al_2O_3	21.45	21.64	0.15	2.12	1.91	3.57	3.99	3.42	1.23	12.73	12.96	14.50
Cr_2O_3	1.33	1.30	0.05	0.32	0.28	0.09	0.76	0.87	0.24	1.49	1.03	0.19
FeO	8.65	11.69	6.06	6.78	7.27	7.26	2.04	2.75	7.58	3.63	2.45	15.93
MnO	0.28	0.70	0.16	0.17	0.20	0.18	0.09	0.11	0.42	0.06	0.00	0.21
MgO	20.57	18.25	35.94	34.01	33.73	33.35	16.33	18.05	19.96	18.25	25.39	15.15
CaO	4.41	4.31	0.12	0.21	0.43	0.25	22.39	19.55	11.46	12.34	0.00	0.00
Na_2O	0.00	0.02	0.00	0.00	0.00	0.00	1.04	1.03	0.26	1.76	0.15	0.20
K_2O	na	na	na	na	na	na	na	na	0.13	0.99	9.60	9.36
P_2O_5	na	na	na	na	na	na	na	na	na	na	na	na
NiO	na	na	na	na	na	na	na	na	na	na	na	na
ZnO	na	na	na	na	na	na	na	na	na	na	na	na
Total	**98.63**	**99.96**	**100.10**	**99.67**	**99.61**	**99.78**	**99.95**	**99.57**	**96.61**	**96.39**	**93.99**	**95.87**
Oxygen	**12**	**12**	**6**	**6**	**6**	**6**	**6**	**6**	**23**	**23**	**11**	**11**
Cation												
Si	2.988	3.000	1.980	1.943	1.941	1.911	1.920	1.936	7.695	6.364	2.937	2.852
Ti	0.034	0.033	0.001	0.001	0.002	0.002	0.009	0.008	0.004	0.042	0.062	0.113
Al	1.828	1.845	0.006	0.087	0.078	0.146	0.170	0.146	0.201	2.133	1.087	1.272
Cr	0.076	0.074	0.001	0.009	0.008	0.002	0.022	0.025	0.027	0.168	0.058	0.011
Fe^{2+}	0.523	0.707	0.174	0.197	0.212	0.211	0.062	0.083	0.864	0.432	0.146	0.992
Fe^{3+}	–	–	–	–	–	–	–	–	0.018	0.000	–	–
Mn	0.017	0.043	0.005	0.005	0.006	0.005	0.003	0.003	0.050	0.007	0.000	0.014
Mg	2.217	1.969	1.843	1.759	1.752	1.727	0.882	0.974	4.142	3.869	2.694	1.681
Ca	0.342	0.334	0.005	0.008	0.016	0.009	0.869	0.758	1.709	1.880	0.000	0.000
Na	0.000	0.003	0.000	0.000	0.000	0.000	0.073	0.073	0.070	0.485	0.020	0.029
K	–	–	–	–	–	–	–	–	0.023	0.179	0.871	0.888
Total cation	**8.03**	**8.01**	**4.01**	**4.01**	**4.01**	**4.01**	**4.01**	**4.01**	**16.80**	**17.56**	**7.87**	**7.85**
Mg#	**0.81**	**0.74**	**0.91**	**0.90**	**0.89**	**0.89**	**0.93**	**0.92**	**1.00**	**1.00**	**0.95**	**0.63**
Cr#	**2.83**	**2.85**	**0.20**	**0.09**	**0.09**	**0.02**	**0.11**	**0.15**	**0.12**	**0.07**	**0.05**	**0.01**
(Na + K)$_{tot}$	–	–	–	–	–	–	–	–	**0.09**	**0.66**	–	–

probably related to diffusion, while no zoning is observed neither in Ca nor in Cr.

In the well-preserved part of the spinel harzburgite sample JB-19-22, amphibole is a slightly chromian pargasite (Cr = 0.15–0.19 p.f.u, Mg# > 0.94 and Al^{iv} = 1.40–1.76 p.f.u). In sample JB-19-21 (phlogopite-chromite harzburgite), amphibole was only observed in the corona that rims the peridotite enclave. It is a nearly pure tremolite with low Cr-content (Cr = 0.02–0.05 p.f.u, Mg# > 0.95, Al^{iv} = 0.20–0.33, Fig. 7f).

Spinel in sample JB-19-22 is a slightly chromian Mg-spinel (Mg# = 0.63–0.66, Cr# = 0.29–0.35, Fig. 7g) with high Ni-content (1250–1500 ppm, Fig. 7h) and low Mn (1240–1365 ppm), Zn (2700–3200 ppm), V (820–950 ppm) and Ti (300–400 ppm) content. By contrast, sample JB-19-21 contains ferroan chromite (Mg# = 0.15–0.40, Cr# = 0.81–0.91) with much lower Ni-content (500–740 ppm) but much higher Zn (up to 7400 ppm), V (1000–1250 ppm), Mn (2600–10 050 ppm) and Ti (4500–6200 ppm) content than spinel of sample JB-19-22.

Finally, mica was only analyzed in sample JB-19-21 (Fig. 7i). The harzburgite core of the sample contains nearly pure, Cr-rich–Ti-poor phlogopite (Mg# = 0.95, Ti = 0.05–0.06 p.f.u, Cr = 0.06 p.f.u). In contrast, the coronas around the enclave contain less magnesian, Ti-rich–Cr-poor biotite (Mg# = 0.62–0.63, Cr < 0.02 p.f.u, Ti = 0.11).

Table 3. Representative EPMA analyses of spinel, chromite and olivine, including trace elements measured with a high intensity electron beam (Batanova *et al.*, 2015). na: not analyzed. The complete set of analyzes is provided in the Supplementary Material.

Tableau 3. *Sélection représentative d'analyses à la microsonde électronique du spinelle, de la chromite et de l'olivine, incluant les éléments traces mesurés avec une forte intesité du faisceau d'électrons (Batanova* et al.*, 2015). na : non analysé. Le jeu de données complet est disponible en matériel supplémentaire.*

Sample	JB-19-21	JB-19-22	JB-19-21	JB-19-21	JB-19-22	JB-19-33
Mineral	*Chr*	*Spl*	*Olivine*	*Olivine*	*Olivine*	*Olivine*
LABEL	*Spl-09*	*Spl-01*	*Ol-07*	*Ol-18*	*Ol-06*	*Ol-07*
Position	core	core	core	rim	core	core
wt% oxides						
SiO_2	0.02	0.00	40.83	39.29	40.80	40.58
TiO_2	0.93	0.06	0.0035	0.0016	0.0010	0.0028
Al_2O_3	4.38	37.75	0.0000	0.0000	0.0000	0.0018
Cr_2O_3	58.96	28.98	0.0268	0.0110	0.0022	0.0028
V_2O_3	0.17	0.12	na	na	na	na
FeO	29.47	18.10	8.79	17.27	9.66	10.78
MnO	0.87	0.18	0.1308	0.7278	0.1455	0.1669
MgO	3.77	14.75	49.54	42.36	48.98	48.11
CaO	na	na	0.0091	0.0052	0.0133	0.0133
P_2O_5	na	na	0.0214	0.0779	0.0136	0.0100
NiO	0.07	0.16	0.4256	0.2446	0.3731	0.3590
ZnO	0.64	0.40	na	na	na	na
Total	**99.29**	**100.50**	**99.78**	**99.99**	**100.00**	**100.02**
Oxygen	**4**	**4**	**4**	**4**	**4**	**4**
Cation						
Si	–	–	1.02	0.97	1.01	1.01
Ti	0.025	0.001	–	–	–	–
Al	0.184	1.268	–	–	–	–
Cr	1.661	0.653	–	–	–	–
Fe^{2+}	0.752	0.343	0.36	0.71	0.40	0.44
Fe^{3+}	0.127	0.089	–	–	–	–
Mg	0.200	0.627	1.60	1.35	1.57	1.54
Total cation	**2.95**	**2.98**	**2.98**	**3.03**	**2.99**	**2.99**
Mg#	**0.90**	**0.34**	**0.91**	**0.81**	**0.90**	**0.89**
Cr#	**0.21**	**0.65**	**–**	**–**	**–**	**0.61**
Trace ppm						
Ni	586	1259	3344	1922	2932	2821
Mn	6766	1365	1013	5637	1127	1293
Cr	–	–	183	75	15	19
V	1155	840	–	–	–	–
Ca	–	–	65	37	95	95
Ti	5570	357	21	10	6	17
Si	90	0	–	–	–	–
Al	–	–	–	–	–	10
P			93	340	59	44
Zn	5158	3213	–	–	–	–
Ni/Mn	0.09	0.92	3.30	0.34	2.60	2.18

6 Whole-rock geochemistry and Nd–Sr isotopes

6.1 Major elements

All the samples have been serpentinized to various degrees during retrogression, but this process is generally considered to induce no or very minor changes in major element composition, and preserves in particular Al_2O_3/SiO_2 and MgO/SiO_2 ratios (Deschamps *et al.*, 2013). Formation of talc during serpentinization may nevertheless be associated with strong chemical modification, notably SiO_2 enrichment (Paulick *et al.*, 2006). Apart from highly retrogressed or altered domains which have been removed before crushing, no
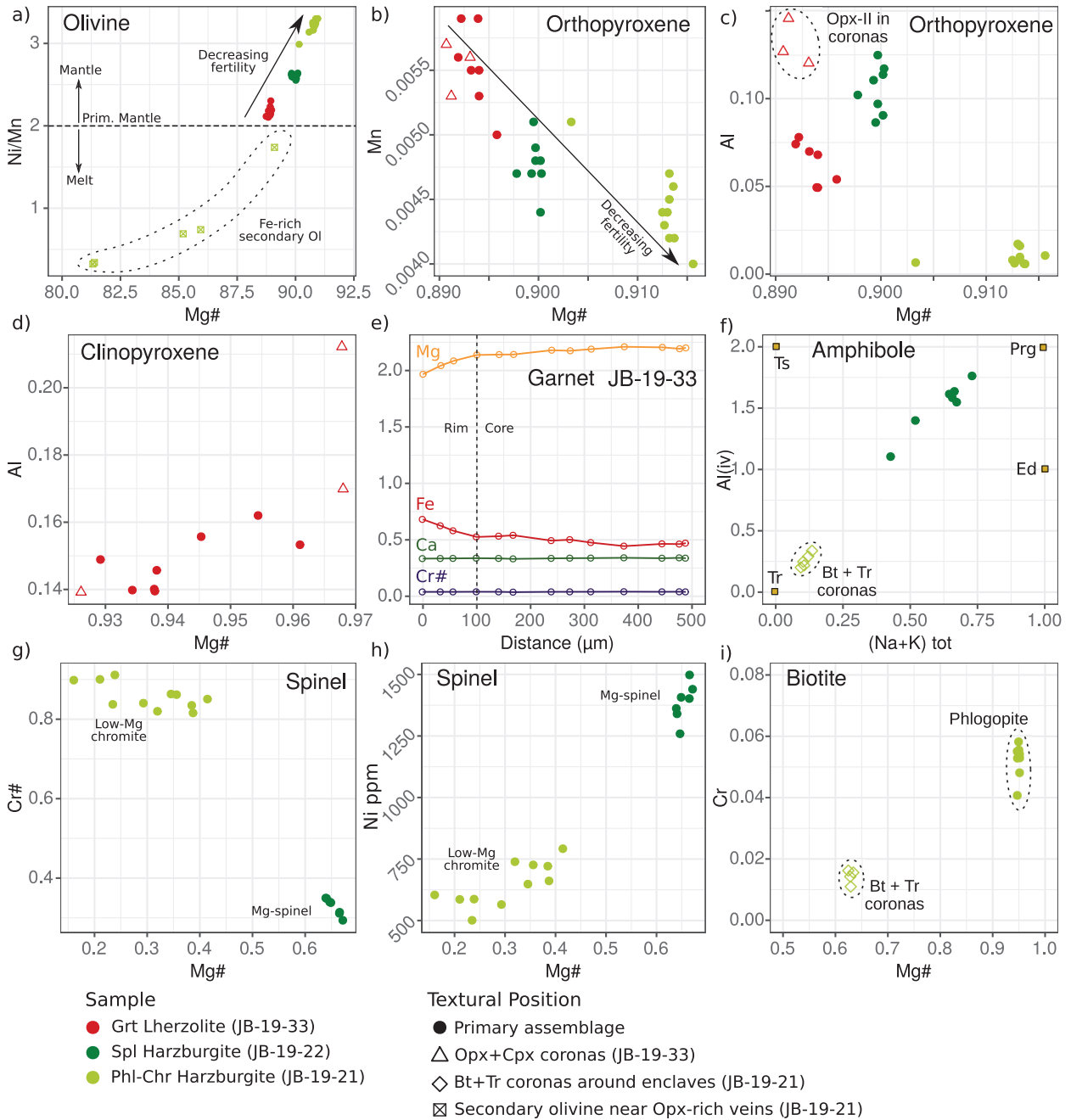
Fig. 7. Mineral compositions in selected representative samples from the three different peridotite groups. Note in particular the negative correlation between Mg# and Ni–Mn content in olivine and orthopyroxene on panel (a and b), and the significant difference in trace element composition between high Mg# and low-Mg# olivine in the phlogopite-harzburgite (JB-19-21). Distinction between mantle and magmatic olivine is after Wang *et al.* (2021). Note also the sharp difference in composition between the Mg–Cr-rich mantle-phlogopite in the core of the harzburgite enclave and biotite formed by melt-rock interaction in the coronas (g). Mineral compositions are expressed in atom per formula unit, and Mg# is expressed as the molar ratio Mg/Mg + Fe²⁺.

Fig. 7. Compositions minérales dans des échantillons représentatifs trois différents groupes de péridotites. Noter en particulier la corrélation négative entre le Mg# et la teneur en Ni-Mn dans l'olivine et l'orthopyroxène (a et b), et la différence significative de composition en éléments traces entre l'olivine riche en Mg et l'olivine pauvre en Mg dans la harzburgite à phlogopite (JB-19-21). Distinction entre olivine mantellique et magmatique d'après Wang et al. (2021). Notez également la forte différence de composition entre les phlogopites mantelliques riches en Mg–Cr dans le cœur de l'enclave de harzburgite et les biotites formées par interaction avec la migmatite dans la couronne réactionelle (g). Les compositions minérales sont exprimées en atome par formule structurale, et Mg# est exprimé comme le rapport molaire Mg/Mg + Fe²⁺.
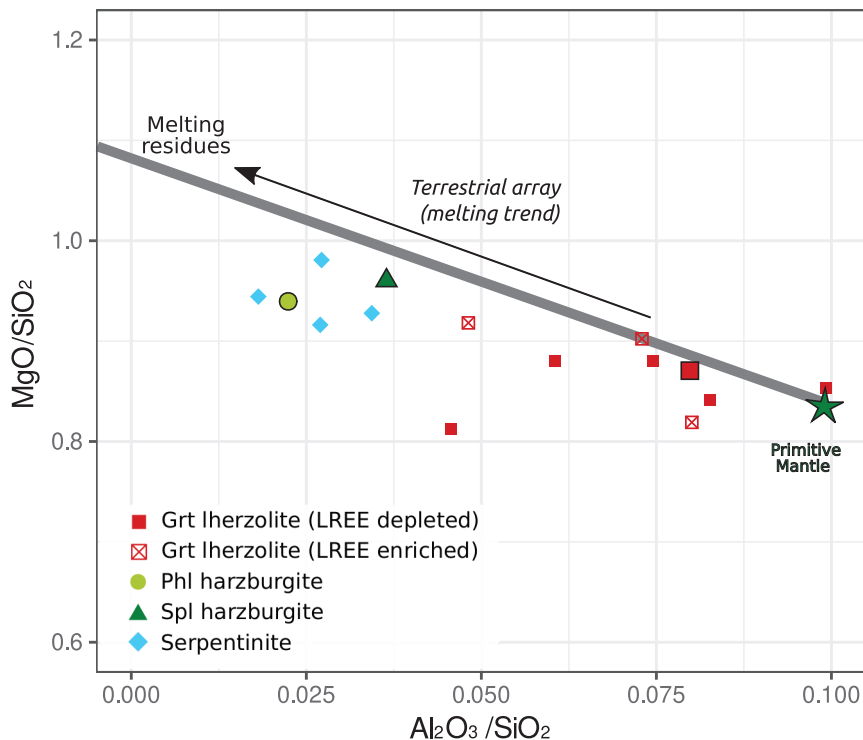
Fig. 8. Whole-rock composition of collected samples recalculated to an anhydrous basis and plotted on the Al_2O_3/SiO_2–MgO/SiO_2 diagram of Paulick *et al.* (2006). All the samples align slightly below the terrestrial mantle melting array (Jagoutz *et al.*, 1979), possibly due to SiO_2 addition during metasomatism (Paulick *et al.*, 2006) or MgO loss during serpentinization. Larger symbols correspond to samples analyzed by electron microprobe.

Fig. 8. *Composition roche totale des échantillons collectés, recalculée sur une base anhydre et reportée sur le diagramme Al_2O_3/SiO_2–MgO/SiO_2 de Paulick et al. (2006). Tous les échantillons s'alignent légèrement en dessous de la ligne « terrestre » (Jagoutz et al., 1979), probablement en raison d'un ajout de SiO_2 pendant le métasomatisme (Paulick et al., 2006) ou d'une perte de MgO pendant la serpentinisation. Les échantillons analysés par microsonde électronique sont mis en évidence par des symboles plus gros.*

talc has been observed in the samples. Therefore, the measured compositions re-normalized to an anhydrous basis (Tab. 1) are considered as representative of the whole-rock compositions before serpentinization. Normalizing to dry composition may induce a bias for the phlogopite/pargasite-bearing samples, which were not completely anhydrous before serpentinization. This bias is however assumed to be small considering the very high loss on ignition (8–10 wt%), which is dominated by serpentine and other volatile-bearing phases formed during retrogression rather than pre-existing metasomatic minerals.

In the Al_2O_3/SiO_2–MgO/SiO_2 diagram (Fig. 8), all peridotite and serpentinite analyses plot slightly below the terrestrial array (melting trend of primitive mantle), which could result from addition of silicic melt or metasomatic SiO_2 addition (Paulick *et al.*, 2006). The clinopyroxene-rich garnet lherzolites are particularly fertile and are characterized by high $Al_2O_3/SiO_2 > 0.04$, low MgO/SiO_2 (0.81–0.91 wt%), and high CaO (1.41–2.69 wt%). By contrast, the serpentinites, the spinel and the phlogopite-chromite harzburgites display low $Al_2O_3/SiO_2 < 0.04$, high MgO/SiO_2 (0.91–0.96) and low CaO (0.28–1.42 wt%wt%), which is more typical of residual harzburgitic mantle that has experienced partial melting (Fig. 8). The phlogopite–chromite harzburgite JB-19-21 is also enriched in K_2O (0.63 wt%) and P_2O_5 (0.12 wt%) relative to the other samples, which all contain less than 0.35 wt% K_2O and P_2O_5 below detection limit (< 0.1 wt%).

Variation in major element composition reflects the mineralogical composition of the peridotites. In particular, the trend in the Al_2O_3/SiO_2–MgO/SiO_2 diagram is consistent with composition of olivine and orthopyroxene, which are more magnesian in the most refractory harzburgites than in the most fertile garnet lherzolite (Figs. 7a and 7b). Furthermore, higher CaO and Al_2O_3 in the lherzolites is consistent with the large abundance of – retrogressed – garnet and clinopyroxene, and higher K_2O and P_2O_5 in sample JB-19-21 is consistent with the presence of phlogopite and apatite.

6.2 Trace elements

Trace element analyses recast on an anhydrous basis are given in Table 4. Large variability is observed in trace element composition, and three main groups are identified based on REE content (Fig. 9a). The first group includes most of the garnet lherzolites, which present LREE-depleted patterns ($La_N/Yb_N = 0.46$–0.96), with HREE content close to or slightly below that of the primitive mantle ($Yb_N = 0.5$–1.1). Samples from this group display no or slightly positive Eu anomaly ($Eu/Eu^* = 1.0$–1.2, where $Eu/Eu^* = Eu_N/(Sm_N.Gd_N)^{1/2}$), and are not particularly enriched in Th ($Th_N/Yb_N = 0.48$–2.12), in contrast to the other groups. The second group includes the spinel and the phlogopite harzburgites, plus three samples of

Table 4. Whole-rock trace element composition recalculated on an anhydrous basis. Key race element ratios normalized to the primitive mantle composition (McDonough and Sun, 1995) have also been calculated. < d.l: values below detection limit. Grt Lrz: Garnet Lherzolite; Spl Hrz: Spinel Harzburgite; Phl Hrz: Phlogopite–chromite Harzburgite; Srp: Serpentinite.

Tableau 4. Analyses roche totale en éléments traces, recalculées sur une base anhydre. < d.l. : valeurs inférieures à la limite de détection. Grt Lrz : Lherzolite à grenat ; Spl Hrz : Harzburgite à spinelle ; Phl Hrz : Harzburgite à phlogopite–chromite ; Srp : Serpentinite.

Sample	JB-19-20	JB-19-23	JB-19-31	JB-19-33	JB-19-34	JB-20-06	JB-20-12	JB-20-13	JB-20-14	JB-19-21	JB-19-22	JB-18-27	JB-19-45	JB-19-48	JB-19-49
Type	*Grt Lrz*	*Grt Lrz*	*Grt Lrz*	*Grt Lrz*	*Grt Lrz*	*Grt Lrz*	*Grt Lrz*	*Grt Lrz*	*Grt Lrz*	*Phl Hrz*	*Spl.Hrz*	*Srp*	*Srp*	*Srp*	*Srp*
As	0.92	90.21	2.12	3.88	3.84	5.81	5.16	1.08	4.07	12.30	2.76	26.93	78.75	496.29	65.25
Ba	22.1	< d.l	21.6	< d.l	< d.l	< d.l	< d.l	< d.l	50.0	171.5	26.9	< d.l	9.6	< d.l	< d.l
Be	< d.l	0.91	0.55	< d.l	0.71	0.26	0.95	0.15	0.49	1.18	0.32	0.16	0.50	0.21	0.09
Bi	< d.l	0.07	0.75	0.09	0.10	0.06	< d.l	0.08	0.26	0.31	1.21	0.12	0.42	1.09	0.13
Cd	0.03	0.03	0.08	0.04	< d.l	0.03	0.03	0.06	0.06	0.07	< d.l	1.89	0.09	< d.l	< d.l
Co	101.9	110.8	97.9	103.5	105.1	101.4	100.3	99.7	111.8	129.2	111.8	121.2	113.6	119.8	81.0
Cr	2718	2803	2426	2499	2563	2598	2710	2871	2723	5674	2705	3038	2815	2772	2675
Cs	1.52	7.90	3.17	1.30	3.65	2.63	2.56	0.66	1.51	4.02	5.96	1.46	3.56	0.47	0.20
Cu	7.33	5.95	8.85	8.51	3.49	6.55	5.69	13.74	14.13			5.59	5.81	< d.l	3.35	< d.l
Ga	3.0	2.2	4.0	3.4	3.1	2.6	3.6	3.6	2.5	2.1	1.9	1.1	1.4	1.5	0.8
Ge	0.85	2.18	1.02	0.88	0.93	0.95	1.01	0.92	0.96	2.13	0.88	1.03	1.20	1.42	1.02
Hf	0.14	0.09	0.32	0.20	0.18	0.19	0.20	0.25	0.31	0.55	0.18	0.05	< d.l	0.13	< d.l
Nb	0.08	0.05	0.37	0.07	0.09	0.06	0.03	0.08	0.37	0.88	0.63	0.06	0.19	0.18	0.08
Ni	1979	2129	1891	1909	2038	2064	2005	1865	2157	2788	2104	2088	2171	2201	2322
Pb	1.57	2.42	1.57	0.58	0.60	11.88	5.97	0.59	4.91	1.84	1.44	3.15	2.62	1.35	< d.l
Rb	1.09	5.68	14.81	2.38	4.15	3.36	4.24	2.52	7.76	34.93	17.31	0.99	17.70	0.29	0.28
Sb	0.07	2.00	0.13	0.12	3.09	2.07	1.07	0.35	0.41	3.78	0.63	0.81	4.66	7.69	9.51
Sc	15.0	11.8	15.2	15.5	15.0	13.1	16.4	19.2	13.0	3.2	12.4	12.4	12.3	10.1	7.5
Sn	< d.l	< d.l	1.64	< d.l	< d.l	< d.l	< d.l	< d.l	0.93	< d.l	0.34	0.66	0.46	0.43	< d.l
Sr	9.7	11.1	8.0	10.0	17.8	12.3	11.6	9.6	29.9	7.0	15.2	13.8	9.0	5.6	6.6
Ta	0.0	0.0	0.0	0.0	0.0	0.0	0.0	0.0	0.0	0.1	0.0	0.0	0.0	0.0	0.0
Th	0.50	0.08	0.65		0.03	0.03	0.08	0.05	0.48	1.24	0.55	0.08	0.04	0.37	0.08
U	0.11	0.05	0.38	0.03	0.02	0.04	0.06	0.11	0.37	0.80	0.32	0.37	0.11	0.10	0.06
V	63.3	46.5	69.4	70.4	65.6	55.9	74.8	79.0	53.4	15.9	41.1	34.0	42.3	35.5	27.0
W	< d.l	3.3	4.3	< d.l	< d.l	< d.l	< d.l	< d.l	< d.l	< d.l	1.3	11.7	1.0	3.0	6.2
Y	2.70	1.92	4.90	3.19	3.16	2.28	3.54	4.36	1.57	2.47	1.28	0.66	0.31	1.16	0.33
Zn	56.8	61.0	68.4	54.4	53.9	59.7	71.5	62.1	72.4	99.9	54.1	87.4	49.3	67.0	62.2
Zr	4.1	2.8	10.8	7.2	6.2	6.7	6.7	8.5	10.4	17.7	6.5	2.2	< d.l	4.8	< d.l
La	0.930	0.293	1.053	0.235	0.210	0.186	0.434	0.329	1.356	1.771	1.949	0.389	0.152	0.750	0.503
Ce	1.866	0.696	2.499	0.762	0.665	0.601	0.999	0.986	4.099	4.206	4.936	0.581	0.397	1.543	0.936
Pr	0.234	0.106	0.367	0.141	0.117	0.110	0.159	0.172	0.658	0.589	0.620	0.088	0.052	0.200	0.118
Nd	1.039	0.526	1.810	0.807	0.665	0.599	0.839	0.895	3.067	2.577	2.266	0.359	0.190	0.833	0.464
Sm	0.291	0.202	0.608	0.298	0.250	0.232	0.317	0.353	0.859	0.615	0.402	0.075	0.043	0.204	0.101
Eu	0.090	0.084	0.158	0.121	0.120	0.102	0.146	0.139	0.176	0.085	0.084	0.018	0.038	0.111	0.082
Gd	0.356	0.252	0.707	0.405	0.362	0.299	0.427	0.497	0.604	0.525	0.270	0.083	0.031	0.196	0.082
Tb	0.064	0.047	0.128	0.075	0.066	0.056	0.086	0.098	0.069	0.079	0.039	0.014	0.005	0.032	0.011
Dy	0.465	0.326	0.839	0.505	0.473	0.404	0.596	0.719	0.311	0.473	0.227	0.091	0.046	0.207	0.062
Ho	0.107	0.074	0.185	0.117	0.111	0.089	0.139	0.166	0.058	0.094	0.047	0.023	0.012	0.046	0.013
Er	0.294	0.216	0.509	0.330	0.317	0.254	0.396	0.477	0.156	0.242	0.131	0.066	0.040	0.126	0.036
Tm	0.049	0.033	0.080	0.053	0.050	0.040	0.061	0.074	0.023	0.037	0.022	0.012	0.007	0.020	0.005
Yb	0.312	0.219	0.532	0.344	0.327	0.267	0.393	0.482	0.164	0.257	0.153	0.085	0.059	0.123	0.035
Lu	0.049	0.036	0.083	0.051	0.055	0.041	0.061	0.076	0.025	0.042	0.027	0.015	0.011	0.019	0.007
$(Th/Nb)_N$	54.857	13.843	14.605		2.671	4.917	21.938	5.354	10.796	11.709	7.288	11.542	1.711	16.961	7.748
$(Th/Yb)_N$	9.328	2.119	7.099		0.484	0.737	1.191	0.644	16.988	27.870	20.825	5.306	3.768	17.542	12.749
$(Th/La)_N$	4.358	2.204	5.000		1.051	1.474	1.500	1.315	2.869	5.635	2.273	1.619	2.030	3.996	1.240
$(La/Yb)_N$	2.140	0.962	1.420	0.490	0.460	0.500	0.794	0.490	5.921	4.946	9.162	3.278	1.856	4.390	10.279

a) REE patterns
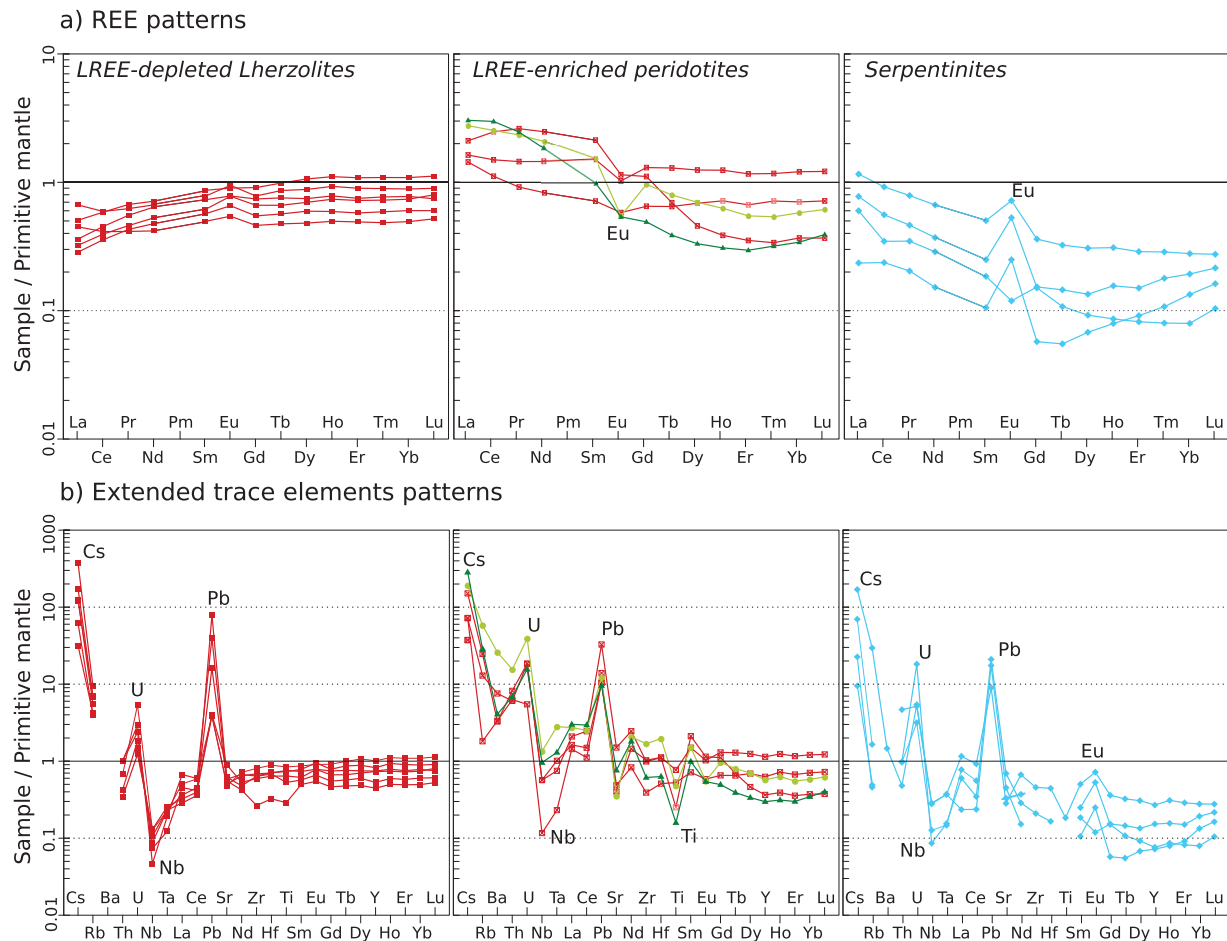

b) Extended trace elements patterns

Fig. 9. Trace element composition of collected samples, normalized to the composition of primitive mantle after McDonough and Sun (1995). Three groups are identified based on their trends in rare earth elements (see description in text). See Figure 8 for the legend.
Fig. 9. *Composition en éléments traces des échantillons collectés, normalisée à la composition du manteau primitif d'après McDonough et Sun (1995). Trois groupes sont identifiés à partir des spectres en terres rares (voir description dans le texte). Légende identique à la figure 8.*

garnet lherzolite, which present similar REE patterns. They display a HREE content similar to samples of the first group ($Yb_N = 0.4–1.2$), but they are strongly enriched in LREE and Th ($La_N/Yb_N = 1.42–9.16$, $Th_N/Yb_N = 7.10–27.87$) and present a negative Eu anomaly ($Eu/Eu^* = 0.46–0.85$). The third group consists of serpentinites. They are all strongly depleted in HREE relative to the primitive mantle ($Yb_N = 0.08–0.28$), and display either U-shaped REE patterns, with depletion in MREE relative to HREE and LREE, or continuous enrichment from HREE to LREE ($La_N/Yb_N = 1.86–10.28$, $Th_N/Yb_N = 3.77–17.54$). With one exception, all the analyzed serpentinites have a positive Eu anomaly (Eu/Eu^* up to 3.2). These three groups share in common a strong enrichment in LILE and other fluid-mobile incompatible elements, in particular Cs, Rb, U and Pb, and strongly negative anomalies in HFSE, in particular in Nb and Ta, independently of their mineral composition or REE and Th content (Fig. 9b). Th_N/Nb_N ratio, which quantifies this anomaly, ranges between 1.71 and 54.86.

6.3 Sr–Nd isotopes

Nine samples have been selected for bulk-rock Sr–Nd isotopic analyses (Tab. 5). However, due to very low Nd content, no Nd isotopic data could be acquired for samples from the LREE-depleted group, and the only available Nd data are from LREE-enriched samples. Initial εNd_i have been recalculated at 330 Ma, which corresponds to the climax of the Variscan collision in the ECM. Variations of ± 20 Ma on the initial age have little effect on recalculated εNd_i ($\pm 0.07–0.23$) compared to the observed variation range. εNd_{330} values cover a large range from slightly positive to strongly negative values (-8.12; $+0.59$). Slight contamination by granitic melt in the migmatite cannot be excluded, which would shift εNd_{330} toward lower values. However, only the freshest part of the enclaves, which did not present macroscopic evidences of melt-rock interaction in the migmatite, has been selected for whole-rock isotopic analyses. Therefore, we consider that the measured whole-rock isotopic compositions are dominated by

Table 5. Whole-rock Sr–Nd isotopic compositions. Initial εNd have been recalculated at 330 Ma, which corresponds to the climax of the Variscan collision in the ECM. Sensitivity of εNdi to variation in initial age is shown by recalculating isotopic compositions at 350 Ma and 300 Ma (values in bracket). Recalculation of initial $^{87}Sr/^{86}Sr$ is hampered by high uncertainty related to high Rb/Sr ratios in certain samples, and possible contamination by fluids or melts in the crust.

Tableau 5. Compositions isotopiques en Sr–Nd sur la roche totale. Les εNd initiaux ont été recalculés à 330 Ma, ce qui correspond au pic de la collision varisque dans les Massifs Cristallins Externes. La sensibilité de εNdi à la variation de l'âge initial est testée en recalculant les compositions isotopiques à 350 Ma et 300 Ma (valeurs entre parenthèses). Le calcul des rapports $^{87}Sr/^{86}Sr$ initiaux est entravé par une forte incertitude, liée à des rapports Rb/Sr élevés dans certains échantillons, et à une contamination possible par des fluides ou des liquides silicatés dans la croûte.

| Sample | Type | Composition (ppm) | | | | Sr isotopes | | Nd isotopes | | | |
		Rb	Sr	Nd	Sm	$^{87}Rb/^{86}Sr$	$^{87}Sr/^{86}Sr$	$^{147}Sm/^{144}Nd$	$^{143}Nd/^{144}Nd$	εNd$_{330}$	εNd$_{[350-310]}$
JB-19-20	*Grt Lrz*	1.09	9.7	1.039	0.291	0.32445	0.70895	0.16938	0.51261	0.59	[+0.78; +0.64]
JB-19-33	*Grt Lrz*	2.38	10.0	0.807	0.298	0.68983	0.70440				
JB-20-12	*Grt Lrz*	4.24	11.6	0.839	0.317	1.05645	0.71017				
JB-20-13	*Grt Lrz*	2.52	9.6	0.895	0.353	0.75968	0.70572				
JB-20-14	*Grt Lrz*	7.76	29.9	3.067	0.859	0.75138	0.71442	0.16924	0.51216	−8.12	[−7.92; −8.06]
JB-19-21	*Phl Hrz*	34.93	7.0	2.577	0.615	14.4460	0.76771	0.14426	0.51224	−5.64	[−5.38; −5.65]
JB-19-22	*Spl.Hrz*	17.31	15.2	2.266	0.402	3.30482	0.72185	0.10713	0.51230	−2.78	[−2.44; −2.89]
JB-19-48	*Srp*	0.29	5.6	0.833	0.204	0.15114	0.71727	0.14816	0.51246	−1.37	[−1.13; −1.37]
JB-19-49	*Srp*	0.28	6.6	0.464	0.101	0.12105	0.71783				

Fig. 10. (a) Isochemical phase diagram computed with PerpleX 6.9.0 (Connolly, 2009). P–T conditions are inferred using the composition quality factor Q$_{cmp}$ (Duesterhoeft and Lanari, 2020), which is computed over the P–T grid for the primary Grt + Opx-I + Cpx-I assemblage (b). Best fit between modeled and measured composition (Q$_{cmp}$ close to 1, in yellow) is obtained around 940–980 °C and 2–4 GPa and is consistent with results obtained by inverse thermobarometry (red lines). Another diagram with P–T estimations obtained from standard composition isopleths is provided in the Supplementary Material. Inverse thermobarometry on Opx-II + Cpx-II coronas around garnet indicate lower temperature of equilibration around 800–850 °C (blue lines). TA98: Taylor (1998); BK90: Brey and Köhler (1990); NG85: Nickel and Green (1985).

Fig. 10. (a) Diagramme de phase (pseudosection) calculé avec PerpleX 6.9.0 (Connolly, 2009). Les conditions P–T sont estimées à l'aide du critère de composition Q$_{cmp}$ (Duesterhoeft et Lanari, 2020), calculé sur l'ensemble sur la grille P–T pour l'assemblage primaire à Grt + Opx-I + Cpx-I (b). Le meilleur ajustement entre la composition modélisée et celle mesurée (indiqué par une valeur de Q$_{cmp}$ proche de 1, en jaune) est obtenu autour de 940–980 °C et 2–4 GPa, et est cohérent avec les résultats obtenus par thermobarométrie inverse (lignes rouges). Un diagramme montrant les estimations P–T obtenues avec la méthode standard (intersection des isoplèthes de composition) est disponible en matériel supplémentaire. La thermobarométrie inverse sur les couronnes secondaires autour du grenat (Opx-II + Cpx-II) indique une température d'équilibre plus basse, autour de 800–850 °C (lignes bleues). TA98: Taylor (1998) : BK90: Brey et Köhler (1990) : NG85: Nickel et Green (1985).

Table 6. Summary of P–T estimates in sample JB-19-33. For inverse thermobarometry, reported P and T are average of several measurements. Reported uncertainties of $\pm 50\,°C$ and $\pm 0.5\,GPa$ are conservative estimates taking into account composition variation and internal calibration uncertainty (Nimis and Grütter, 2010).

Tableau 6. Résumé des estimations P–T sur l'échantillon JB-19-33. Pour la thermobarométrie inverse, les valeurs de P et T reportées, sont des moyennes obtenues à partir de plusieurs mesures dans chaque domaine. Les incertitudes rapportées de $\pm 50\,°C$ et $\pm 0.5\,GPa$ sont des estimations conservatrices prenant en compte les variations de composition et les incertitudes internes des différents thermobaromètres (Nimis et Grütter, 2010).

Assemblage	Inverse thermobarometry			PerpleX	
	P (GPa)	T (°C) TA98	T (°C) BK90	T (°C)	P (GPa)
Opx-I + Cpx-I + Grt	3.0 ± 0.5 (NG85)	973 ± 50	1137 ± 50	940–980	2.0–4.0
Opx-II + Cpx-II (coronas)	1.0 (assumed)	827 ± 50	803 ± 50	nd	0.8–1.3

the peridotite component, and are thus representative of the Variscan mantle composition.

In contrast, Sr isotope data are more difficult to interpret. Measured $^{87}Sr/^{86}Sr$ ratios range from 0.7057 to 0.7677, with highest values measured in the harzburgites (0.7218–0.7677) and in the serpentinites (0.7173–0.7178). Recalculation of initial isotopic composition at 330 Ma may be flawed by late alteration, in particular in the serpentinites, which present high $^{87}Sr/^{86}Sr$ ratios. Furthermore, high Rb/Sr ratios (17 to 35, Tab. 5) in the phlogopite-bearing samples make recalculation of initial $^{87}Sr/^{86}Sr$ very sensitive to even small analytical errors on Rb or Sr contents or age variations. Thus, the Sr isotopic compositions cannot be easily interpreted in terms of mantle processes, and we will not discuss these results further.

7 Thermobarometry

The P–T evolution of the garnet lherzolites has been constrained using inverse thermobarometers based on equilibrium between garnet, clinopyroxene and orthopyroxene. Among the collected samples, only JB-19-33 preserved a complete assemblage with these three phases. P–T conditions have therefore been estimated only on this sample. Two metamorphic stages can be constrained: (i) a first stage in the garnet stability field, which we constrained using the composition of garnet, Opx-I and Cpx-I; (ii) a lower P stage in the spinel stability field, which we constrained using the composition of Opx-II–Cpx-II pairs in the coarse-grained coronas around the kelyphites. We only used composition data acquired in the core of largest grains (ca. 200 μm), which are the least affected by post-growth diffusion. As pointed out by Nimis and Grütter (2010), many formulations of thermobarometric equations commonly used for mantle rocks are not internally consistent and may yield biased results, even in well-equilibrated samples. We followed their recommendations and used the Al-in-Opx barometer of Nickel and Green (1985) (NG85) in combination with the two-pyroxene thermometer of Taylor (1998) (TA98) and the Ca-in-Opx thermometer of Brey and Köhler (1990) (BK90) which have proven to yield the most robust results. Furthermore, these thermobarometers do not rely on Fe–Mg partitioning between co-existing minerals, which is particularly sensitive to diffusion resetting (Carlson, 2006; Cherniak and Dimanov, 2010).

Inverse thermobarometry has been completed by thermodynamic modeling with PerpleX 6.9.0 (Connolly, 2009), using the thermodynamic database of Holland and Powell (2011) and the set of solution models from Jennings and Holland (2015) developed for phase relations in peridotite in the composition space $NaO–CaO–FeO–MgO–Al_2O_3–SiO_2–Cr_2O_3$. All iron was assumed to be ferrous (no Fe^{3+}), and the bulk composition of sample JB-19-33 recalculated on an anhydrous basis was used in input. All P–T results are summarized in Table 6. The phase diagram computed with PerpleX is shown in Figure 10a. The primary assemblage composed of olivine, garnet, clinopyroxene and orthoproxene is stable over a large P–T range above 1.3–2.0 GPa, while spinel appears at lower P between 0.8 and 1.3 GPa. Equilibration conditions of garnet, Cpx-I and Opx-I has been assessed by computing the composition quality factor Q_{cmp} of Duesterhoeft and Lanari (2020) over the whole P–T grid (Fig. 10b). Q_{cmp} gives the match between modeled and measured mineral composition in function of P and T, using the same mineral compositions as those used for inverse thermobarometry. The closer Q_{cmp} is to 1 (yellow shades in Fig. 10b), the better the match. The best composition match ($Q_{cmp} > 0.95$) is obtained for P between 2.0 and 4.0 GPa and T between 940 and 980 °C (Fig. 10b). Inverse thermobarometry using the NG85 and TA98 calibrations yields a comparable estimate for the primary assemblage at P = 3.0 GPa and T = 973 °C. Internal calibration uncertainty of these thermobarometers can realistically be assumed to be around ± 0.5 GPa for P and ± 50 °C for T (Nimis and Grütter, 2010) However, assuming the same pressure (3.0 GPa), the Ca-in-Opx thermometer (BK90) yields higher T at 1136 °C. In contrast, Opx-II–Cpx-II pairs in the coronas yield consistent T of 827 ± 50 °C for the TA98 two-pyroxene thermometer and 803 ± 50 °C for the BK90 Ca-in-Opx thermometer, assuming P = 1.0 GPa.

By contrast with the lherzolites, spinel/phlogopite-chromite harzburgites lack of garnet and clinopyroxene, which prevents the use of classical thermobarometers. Moreover, these samples display clear evidence of modal metasomatism, which makes the identification of equilibrium assemblages for thermobarometry more challenging. Therefore, no P–T estimates have been obtained on these samples. Lack of garnet nevertheless indicates equilibration below the spinel/garnet transition. However, according to Ziberna *et al.* (2013), this transition may be significantly shifted up to > 5 GPa in

Cr-rich depleted harzburgites. Therefore, lack of garnet in the metasomatized harzburgites does not provide any information about initial P, which may well be in the same range as that of the garnet lherzolites.

8 Discussion

8.1 Chemical overprint of enclaves in the crust

The relatively small (< 1 m) peridotite enclaves hosted in migmatites have experienced significant chemical overprint, first at HT conditions in the partially molten crust, and later by low-T fluid addition during retrogression. Precise characterization of this late overprint is needed before discussing more extensively about the mantle composition and mantle processes recorded by these enclaves. Chemical interaction with the migmatite host, either at supra-solidus or sub-solidus conditions, is evidenced by the development of reaction coronas at the contact of the enclaves. However, many enclaves display sharp contact with the migmatites, or are surrounded only by a thin rim of biotite and/or hornblende (Figs. 3a, 3b and 3g), which suggests that chemical interactions with the host have been restricted to a thin outer rim, with little effect in the core of enclaves. Migmatite-peridotite interactions are however particularly visible around some harzburgite enclaves, especially on sample JB-19-21, which is surrounded by spectacular radial coronas composed of biotite + tremolite (Figs. 3c and 3d). Furthermore, Opx-rich veins observed in this sample (Fig. 4a) are interpreted as a product of the reaction Ol + Liq 1 → Opx + Liq 2, in which primary olivine is dissolved by a relatively SiO_2-rich melt (Liq 1), producing orthopyroxene and a more mafic melt (Liq 2). These veins could therefore indicate reaction of the peridotite with granitic liquid in the migmatite. However, such reactions only affected centimeter-wide domains, as shown by the distribution of olivine grains with Fe-rich rims, which are restrained to the immediate vicinity of Opx-rich veins. Since both the coronas and the metasomatic veins have been carefully removed by cutting before doing geochemical analyses, they should only marginally affect the results of the geochemical analyses.

Serpentinization and other low T retrogression reactions occurred to various degrees in all the collected samples, and resulted in significant addition of volatile components (Loss on Ignition (LOI) up to 13 wt%). However, it does not seem that these reactions have significantly affected the composition of minerals. In sample JB-19-21 (phlogopite harzburgite), Fe–Mg–Mn zoning previously developed in olivine was not modified by the development of the serpentine mesh (Fig. 6f), which suggests little or no effect of serpentinization on olivine composition. Fluid-addition does not seem to be associated either with strong modification of the whole-rock trace element and isotopic composition. Positive anomalies in some large ion elements mobile in crustal fluids (U, Pb, Cs) are observed in all samples, independently of the volatile content in these samples, as shown with U/Th plotted against LOI in Figure 11. Two serpentinite outliers with high LOI however display high U/Th relative to other samples, which might be the result of U addition by high U/Th crustal fluids. Negative HFSE anomalies ($Th_N/Nb_N > 1$), LREE enrichment relative to HREE (La_N/Yb_N) and Nd content are also not correlated with the LOI

(Fig. 11), which suggest that the main geochemical features of the peridotites and serpentinites were acquired before serpentinization. Moreover, the strongly negative anomalies in HFSE correspond to Nb and Ta contents well below the primitive mantle composition for most of the samples (Fig. 9b). Thus, even accounting for possible addition of La, Th and U by crustal fluids, these anomalies likely existed before the chemical overprint in the crust.

8.2 P–T evolution of the garnet lherzolites

The primary Grt + Cpx-I + Opx-I assemblage in sample JB-19-33 correspond to an initial equilibration stage of the lherzolites in the garnet field, estimated at $973 \pm 50\,°C$ and $3.0 \pm 0.5\,GPa$ using the NG85 + TA98 thermobarometers, which is consistent with estimation obtained by forward thermodynamic modeling (2–4 GPa, 940–980 °C). However, there is quite a large discrepancy between the TA98 two-pyroxene and the BK90 Ca-in-Opx thermometer, which yields T ca. 150 °C difference. This discrepancy cannot be explained solely by internal uncertainties of the respective calibrations, but more probably results also from composition resetting by diffusion after mineral growth. This may explain for instance the relatively large spread in Mg# and Ca observed for clinopyroxene (Fig. 7d, Table S1). In contrast, Al content in Opx presents little dispersion (Fig. 7c), which suggests little or no diffusion has occurred. We therefore consider the Al-in-Opx barometry is quite robust. Taking the TA98 and BK90 as respectively lower and upper estimates for T, and considering the dependence in T of the NG85 barometer, we estimate that the initial equilibration stage occurred around 970–1140 °C and 3.0–4.0 GPa.

Formation of kelyphites is indicative of a second metamorphic recrystallization stage at lower pressure. Kelyphitization results from reaction between garnet and olivine in the spinel stability field, following the reaction Grt + Ol (+H_2O) → Opx + Cpx + Spl (+Amp) (Godard and Martin, 2000; Obata, 2011), which occurred between 1.3 and 0.8 GPa according to our thermodynamic calculations (Fig. 10). The coarse-grained Opx-II + Cpx-II coronas developed concomitantly with the kelyphite (Obata, 2011), and constrain T between 800 and 850 °C during decompression using the TA98 and BK90 thermometers. Finally, the formation of plagioclase-bearing symplectites around garnet relics indicates further decompression in the plagioclase stability field below ca. 0.8 GPa. Transformation of the kelyphites into coarser symplectites and eventually into a polygonal assemblage of orthopyroxene + clinopyroxene ± spinel ± amphibole (Fig. 4b) is a process indicative of static recrystallization at relatively high T conditions > 800 °C (Obata, 2011). Resulting textures are very similar to annealing textures observed in garnet-clinopyroxene HP mafic granulites of the Oisans–Pelvoux Massif (Jacob *et al.*, 2022), which have experienced an overprint at similar P–T conditions (0.6–0.9 GPa; 800–870 °C) during the late Variscan collisional stages (ca. 310–295 Ma). These textures therefore suggest that the lherzolite enclaves have remained in the lower crust at T > 800 °C, following the first stage of decompression that led to garnet breakdown.
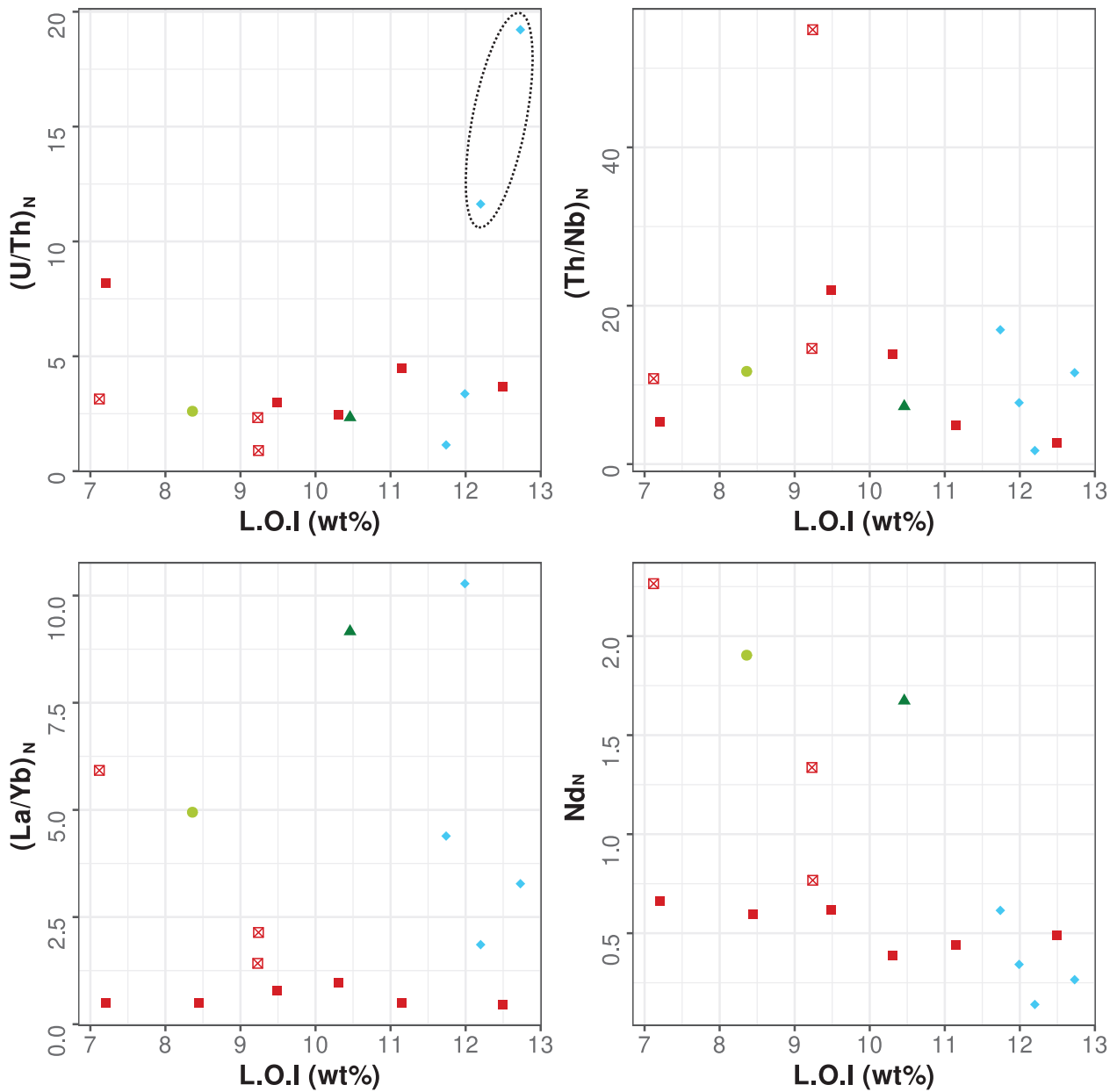
Fig. 11. Whole-rock (U/Th)$_N$, (Th/Nb) $_N$, (La/Yb)$_N$ and Nd$_N$ normalized to the primitive mantle composition in function of the loss on ignition (LOI). LOI is considered as a proxy for fluid addition during retrogression in the crust (mostly serpentinization). Lack of correlation with the LOI ((U/Th)$_N$, (Th/Nb)$_N$, (La/Yb)$_N$) or slightly negative correlation (Nd) suggests that late fluid-addition during retrogression had little effect on whole-rock trace element compositions. Two serpentinite outliers with high (U/Th)N (contoured spots) might have nevertheless experienced significant contamination by fluid. See caption of Figure 8 for the legend. Primitive manle composition after McDonough and Sun (1995).
Fig. 11. *Sélections de paramètres géochimiques sur roche totale (U/Th) $_N$, (Th/Nb)$_N$, (La/Yb)$_N$ et Nd$_N$ (composition normalisée au manteau primitif) en fonction de la perte au feu (LOI). Celle-ci est utilisée comme un indicateur de l'intensité des réactions de rétrogression tardives (serpentinisation principalement), associées à un fort apport de fluide. L'absence de corrélation avec la LOI ((U/Th)$_N$, (Th/Nb)$_N$, (La/Yb)$_N$) ou la présence de corrélation légèrement négative (Nd) suggère que l'apport tardif de fluides pendant la rétrogression a eu peu d'effets sur la composition en éléments traces de la roche totale. Légende identique à la figure 8. Composition du manteau primitif d'après McDonouh and Sun (1995).*

8.3 A refractory mantle refertilized by melts and fluids

Geochemical and mineralogical investigations of the peridotites and serpentinites reveal significant decoupling between major, trace elements and mineral compositions, which we interpret as the result of metasomatic overprint of variably melt-depleted refractory mantle. Initial melt depletion is inferred from whole-rock mineralogy, Al_2O_3/SiO_2 and MgO/SiO_2 compositions, which present large variations from very fertile (high Al_2O_3/SiO_2, cpx-rich) garnet lherzolites to refractory (low Al_2O_3/SiO_2, cpx-poor to cpx-free) harzburgites and serpentinites (Fig. 8). These variations are furthermore consistent with the composition of olivine and orthopyroxene, which display increasing Mg# and Ni and decreasing Mn from the more fertile to the more refractory samples. Finally, even in the most fertile lherzolites, LREE depletion suggests they originally derive from a refractory mantle.

The variable degrees of melt-depletion are however completely decorrelated from the whole-rock trace element compositions. Indeed, largest enrichment in incompatible elements, in particular LREE, Rb, Ba and Th are observed in the refractory harzburgites, while the more fertile lherzolites are depleted in LREE relative to HREE (Fig. 7). Selective enrichment in some LILE (Cs, Rb, U, Pb) relative to HFSE (Nb–Ta) is also observed independently of the mineral and whole-rock composition of the samples, and thus marks a cryptic metasomatic overprint. Some samples also record modal metasomatism, as evidenced by the presence of volatile-bearing phases like phlogopite and pargasite in the refractory harzburgites. In the lherzolites, hydrous minerals (pargasite) are also found, but they are mostly located in former garnet sites (kelyphites or polygonal mosaic assemblages), and may be related to retrogression in the crust rather than mantle metasomatic processes. However, the tiny graphite-bearing inclusions found in garnet relics (Fig. 5) suggest the presence of reduced C–O–H fluids during garnet crystallization. Therefore, it is possible that crystallization of garnet-clinopyroxene-rich assemblages in the LREE-depleted lherzolites was catalyzed by the presence of these reduced fluids.

Similar decoupling between major and trace elements content in orogenic mantle rocks has been widely documented throughout the Variscan Belt (Scambelluri *et al.*, 2006; Medaris *et al.*, 2015; Kubeš *et al.*, 2022). It has commonly been interpreted as the result of an early phase of partial melting, followed by one or multiple phases of metasomatic overprint that led to selective enrichment of the bulk rock in some melt or fluid-mobile trace elements (Medaris *et al.*, 2015; Kubeš *et al.*, 2022). The initial refractory character of the mantle rocks may either indicate derivation from a subducted oceanic lithosphere (Kubeš *et al.*, 2022), or point toward old (possibly Proterozoic) partial melting events in the sub-continental mantle (Medaris *et al.*, 2015). Decoupling between major and trace element composition may result from limited metasomatic influx, which would only produce selective enrichment in specific elements mobile in the metasomatic phase, leaving the initial major element characteristics of the bulk rock largely unmodified. Such a case has been documented by Borghini *et al.* (2018) in mantle eclogites from the Granulitgebirge (NW Bohemian Massif). In these rocks, percolation by felsic melts rich in Cs, Li, B, Pb, Rb, Th, and U is evidenced by the presence of tiny crystallized melt inclusions in garnet, while the bulk rock only recorded very limited enrichment in these elements.

Two different metasomatic trends (subsequently referred to as type-I and type-II) are recorded in the Pelvoux mantle enclaves, which variably affected the different samples: all of them present variable enrichment in LILE (Cs, Rb, U, Pb) relative to Nb and Ta (type-I), while only the harzburgites and some lherzolites are enriched in incompatible LREE and Th (type-II). This dichotomy appears more clearly when plotting Th/Nb (amplitude of Nb anomaly) against Th/Yb (enrichment in incompatible elements relative to HREE). The LREE-depleted lherzolite samples are aligned along a very steep trend (Fig. 12), which indicates increasing Nb anomalies at nearly constant Th/Yb (type-I). In contrast, the LREE-enriched samples are generally more scattered and define a much shallower trend (type-II), which indicates significant enrichment in incompatible elements (Th and LREE) relative to more incompatible ones (HREE), without additional fractionation of LILE relative to Nb and Ta. We interpret these two trends as the result of interactions with different types of fluids or melts, which present different affinities with LREE relative to HREE and LILE relative to HFSE.

The signature of type-I metasomatism is very similar to subduction-related metasomatism, which as been extensively discussed in the literature (*e.g.* Baier *et al.*, 2008; Hermann and Rubatto, 2009; Zheng, 2019). Strong enrichment in LILE relative to Nb and Ta in the metasomatic phase is probably related to melting and/or dehydration at UHP conditions (> 2.5 GPa) of subducted metasediments, in which the stability at HP of phengite, rutile, allanite and monazite exerts a strong control on LILE, Th, LREE and HFSE content of the fluid or melt produced (Hermann and Rubatto, 2009). This type of signature is very common in Variscan mantle (U)HP rocks (Scambelluri *et al.*, 2006; Medaris *et al.*, 2015; Borghini *et al.*, 2018, 2020; Kubeš *et al.*, 2022), which suggests that metasomatism mainly resulted from percolation by silicic melts released during Variscan subduction. This is furthermore confirmed by Lu–Hf and Sm–Nd garnet ages of some metasomatized garnet peridotites which point toward Devonian–Carboniferous age of metasomatism and UHP metamorphism (Tumiati *et al.*, 2003; Ackerman *et al.*, 2020; Kubeš *et al.*, 2022).

Type-II metasomatism presents distinctive characteristics, which can be investigated with more details using mineral compositions and petrographic observations in the phlogopite-chromite harzburgite (sample JB-19-21), one of the most LREE-enriched samples (Fig. 9). Petrographic relations in this sample show that metasomatism is associated with coeval crystallization of phlogopite, chromite and apatite. Composition of low-Mg# chromite, which is poor in compatible Ni, and comparatively richer in more incompatible Ti and Mn (Figs. 7g and 7h, Tab. 3), suggests it crystallized from a melt phase. We therefore suggest that type-II metasomatism was driven by percolation of the harzburgite by a hydrous silicate melt rich in K, P, Cr and LREE. This signature, which is characterized by simultaneous enrichment in compatible (Cr) and incompatible elements, is typical of ultrapotassic magmas like lamproites or lamprophyres (Foley *et al.*, 1987). It appears that similar ultrapotassic magmas are quite widespread in the Variscan basement of ECM (Debon *et al.*, 1998) and other Variscan Massifs of Western and Central Europe. With their more
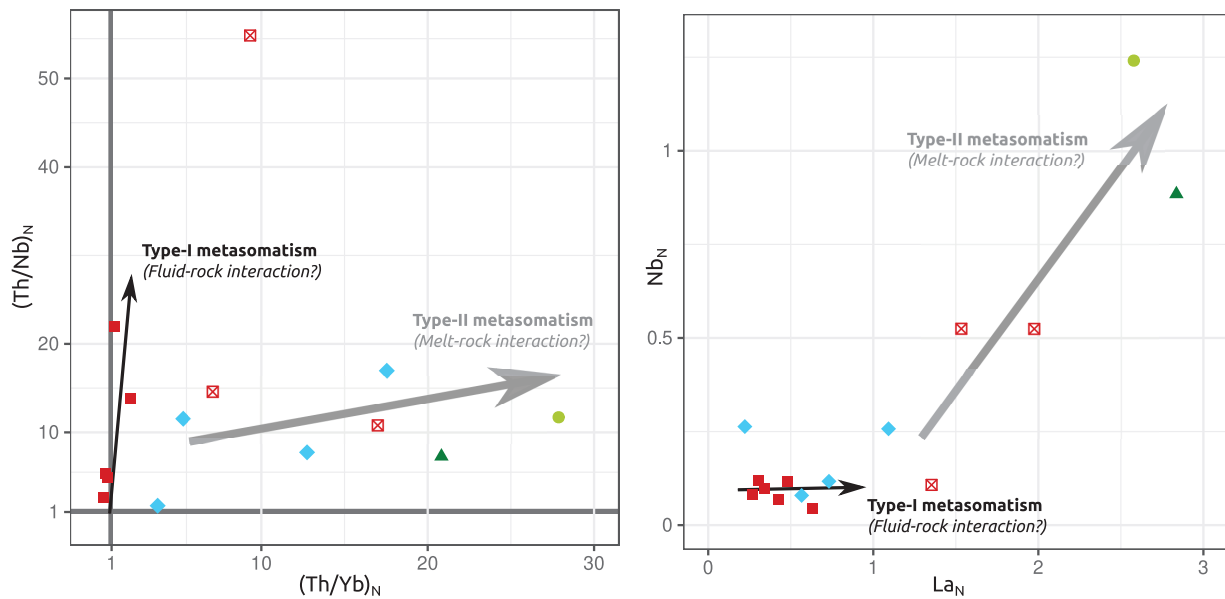
Fig. 12. $(Th/Nb)_N$ *vs.* $(Th/Yb)_N$ diagram (a), and Nb_N *vs.* La_N diagram (b) showing the two metasomatic trends (type-I and type-II) observed in the samples. Compositions are normalized to the primitive mantle of McDonough and Sun (1995), to show the relative evolution of the different groups from this reference. Type-I metasomatism is characterized by increasing HFSE anomaly with little or no fractionation of incompatible elements (LREE + Th) relative to HREE. This corresponds to an increase in $(Th/Nb)_N$ at constant $(Th/Yb)_N$ in Figure 12a, and to an increase in La at constant Nb in Figure 12b. In contrast, type-II metasomatism is characterized by strong enrichment in incompatible elements without fractionating fluid-mobile LREE and fluid-immobile HFSE. This corresponds to an increase in $(Th/Yb)_N$ in Figure 12a, and to a correlated increase in La and Nb in Figure 12b. According to Paulick *et al.* (2006), these two trends are indicative of fluid-rock and melt-rock mantle interaction for type-I and type-II metasomatism, respectively. See caption of Figure 8 for the legend.

Fig. 12. *Diagramme $(Th/Nb)_N$ vs. $(Th/Yb)_N$ (a) et Nb_N vs. La_N (b), montrant les deux tendances métasomatiques observées dans les échantillons (type-I et type-II). Les compositions sont normalisées par rapport au manteau primitif, afin de montrer l'évolution relative des différents groupes à partir de cette référence. Le métasomatisme de type-I est caractérisé par une augmentation des anomalies en HFSE avec peu ou pas de fractionnement des éléments incompatibles (LREE + Th) par rapport aux HREE. Cela se traduit par une augmentation du rapport $(Th/Nb)_N$ sans modification majeure du rapport $(Th/Yb)_N$ (Fig. 12a), et par une augmentation de la teneur en La sans évolution notable de la teneur en Nb (Fig. 12b). À l'inverse, le métasomatisme de type II est caractérisé par un fort enrichissement en éléments incompatibles, sans fractionnement notable en fonction de la mobilité dans les fluides aqueux (LREE vs. HFSE). Cela correspond à une augmentation du rapport $(Th/Yb)_N$ (Fig. 12a), et à une augmentation corrélée de teneurs en La et en Nb (Fig. 12b). D'après Paulick et al. (2006), ces deux tendances sont les marqueurs respectifs d'interaction du manteau avec un fluide aqueux (type-I) et avec un liquide magmatique (type II). Légende identique à la figure 8.*

differentiated counterparts (Mg–K-rich monzodiorite to qtz-monzonite and mela-syenites), they collectively form a magmatic series referred to as durbachites (Von Raumer *et al.*, 2014; Moyen *et al.*, 2017; Soder and Romer, 2018). These durbachites presumably derived from melting of a metasomatized mantle source, enriched by melts derived from a subducted mature continental crust (Janoušek and Holub, 2007; Janoušek *et al.*, 2019, 2020). We therefore speculate that type-II metasomatism is related to percolation in the mantle of the primary magmas from which the durbachites are derived. This hypothesis is supported by experimental work of Foley and Pertermann (2021), who produced a phlogopite harzburgite composition similar to our sample by dynamic percolation of lamproite melt into a garnet peridotite at ca. 3.0 GPa. Finally, the very low εNd_i measured in the phlogopite harzburgite sample is also similar to that of durbachites (Janoušek *et al.*, 2019) and confirms involvement of mature continental material in the source of the metasomatic melts. Variable Nd isotopic signatures ($-8.12 < \varepsilon Nd_i < +0.59$) in the LREE-enriched peridotites suggest that the extent of type-II metasomatism was spatially very heterogeneous, and probably focused along localized melt migration pathways.

8.4 Geodynamic considerations

The ultramafic enclaves from the Pelvoux Massif display a large petrographic variety, and thus probably sample different mantle levels in the garnet and spinel stability field, which were variably affected by metasomatic overprint. UHP conditions recorded in the garnet lherzolite (3.0–4.0 GPa; 970–1140 °C) exceed by far the peak-P conditions of crustal eclogites and HP granulites from the ECM, which are typically between 1.4 and 1.8 GPa (Ferrando *et al.*, 2008; Jouffray *et al.*, 2020; Jacob *et al.*, 2021, 2022; Vanardois *et al.*, 2022). The MP–HT conditions associated with decompression in the spinel field (0.8–1.3 GPa and 800–850 °C) are however quite consistent with the granulite-facies overprint (0.6–0.9 GPa; 800–870 °C) recorded in mafic HP granulites from the Pelvoux Massif, which presumably occurred during the late collisional stages around 325–300 Ma (Jacob *et al.*, 2022). Because of the contrasted P–T evolution, we suggest that the peridotite enclaves were incorporated in the lower crust only during the late stages of the Variscan collision in the ECM (ca. 325–300 Ma), and are not pre-orogenic enclaves.

Decompression of the garnet lherzolites from > 3 GPa to 0.8–1.3 GPa requires significant vertical uplift of at least 50–70 km, assuming lithostatic pressure and a density of 3300 kg.m^{-3} for the lithospheric mantle. However, the exact mechanism for vertical transport of the mantle enclaves remains unclear. Buoyancy-driven exhumation in a subduction channel, or incorporation as tectonic slices in the downgoing continental slab is commonly suggested to explain the presence of mantle enclaves in crustal units (Guillot *et al.*, 2009; Brueckner *et al.*, 2010; Malatesta *et al.*, 2012). However, the Pelvoux Massif lies hundreds of kilometers south of the main Variscan (Saxo-Thuringian/Rheic) subduction zones (Fig. 1), and there is no clear evidence of a former subduction channel preserved in the ECM (Jacob *et al.*, 2021, 2022). Either a subduction was active in the ECM during the early orogenic stages, and was then dismembered by subsequent tectonics and magmatism, forming a "cryptic suture zone" (Schulmann, Lexa *et al.*, 2014; Jouffray *et al.*, 2020), or such a subduction never existed, and alternative mechanisms have to be involved. In the Moldanubian Zone of the Bohemian Massif, "relamination" mechanisms have been suggested to explain the presence of (U)HP units far from the plate interface. These (U)HP units consist of felsic garnet-kyanite-bearing granulites with relics of coesite and/or diamond (Kotková *et al.*, 2011; Perraki and Faryad, 2014), which contain numerous bodies of garnet peridotites and other UHP mantle rocks (Medaris *et al.*, 2005). It is suggested that these units represent buoyant *mélanges* derived from the slab/mantle wedge interface, which were exhumed by diapiric ascent far behind the subduction front, and eventually incorporated into the overlying lower crust. This relaminated lower crust would have then been locally extruded by up-doming (Janoušek and Holub, 2007; Lexa *et al.*, 2011; Schulmann, Catalán *et al.*, 2014). This mechanism has been corroborated by recent thermomechanical modeling (Maierová *et al.*, 2018, 2021), and could be a viable explanation to the presence of mantle enclaves in the lower crust of ECM, far from the subduction trench. Furthermore, it is rather consistent with (i) the extent of metasomatism observed in the enclaves, and (ii) the sampling of different mantle domains at different depths. However, as opposed to the Bohemian Moldanubian Zone, no evidences of UHP conditions in the felsic crust have been found so far. It is therefore still not clear whether the felsic migmatitic host has experienced such extreme conditions. Recent tomographic reconstruction of the crust and upper mantle of the Western and Central Alps indicates the presence of a low-velocity anomaly in the lower crust below the ECM (Nouibat *et al.*, 2022), which might sign the presence of relaminated felsic material. However, extrusion of this lower crust may have been less efficient than in the Bohemian Massif, which would explain the scarcity of mantle enclaves and the lack of large UHP felsic granulite units in the ECM.

Extensive metasomatic interactions with hydrous melts and/or fluids recorded in the ultramafic enclaves are very likely related to slab/mantle interactions during the Variscan orogeny, although we lack of geochronological data to constrain precisely the age. Indeed, older mantle-derived magmatism in the ECM does not present any evidence of mantle enrichment. In particular, Cambrian–Ordovician tholeiitic magmatism, which is widespread in the ECM, consists only of N/E-MORBs with positive εNd$_i$ between +6 and +8 indicative of a depleted mantle source (Paquette *et al.*, 1989). Thus, the mantle below the ECM prior to the Variscan orogeny was probably mostly composed of depleted, refractory harzburgitic material. The initial melt-depletion event inferred from whole-rock and mineral compositions of the peridotites may be related to this widespread magmatic event, although older depletion events are not excluded. The isotopic and trace element enrichment observed in the peridotite enclaves was necessarily acquired later, more probably during Variscan subduction and collision. This is in good agreement with the metamorphic and metasomatic evolution of other Variscan orogenic peridotites. Dating of garnet in lherzolites from the Bohemian Massif (Kubeš *et al.*, 2022) and from the Ulten Zone (Tumiati *et al.*, 2003) yield indeed Carboniferous ages (ca. 340–330 Ma), which points toward a widespread metasomatic event in the mantle occurring during the Variscan collisional stages. This age is very similar to the age of emplacement of the durbachite magmas (Debon *et al.*, 1998), which clearly suggests a connection between this peculiar magmatism and metasomatism observed in mantle rocks.

9 Conclusion

Enclaves of peridotites and serpentinites discovered in exhumed lower and mid-crustal domains in the Oisans–Pelvoux and Belledonne Massif provide insight into the composition and evolution of the Variscan mantle in the ECM. Petrological and geochemical diversity among the enclaves mark the important heterogeneity of the mantle domain from which they derive. Thermobarometric estimations indicate provenance of these enclaves in the upper mantle wedge or the overlying lithospheric mantle. Refractory compositions, characterized in particular by high MgO/SiO$_2$ and low Al$_2$O$_3$/SiO$_2$ in the whole-rock and high Mg# and Ni-content in olivine, mark an early melt-depletion event, presumably related to the widespread Cambrian–Ordovician magmatism recorded all across the Variscan Belt. Depleted mantle domains were variably metasomatized by a LILE-rich phase, probably derived from a Variscan subduction zone, which produced selective enrichment in Cs, Rb, U, Pb relative to less mobile Nb and Ta. Some samples display in addition modal metasomatism (crystallization of phlogopite and/or pargasite with accessory chromite and apatite), associated with a strong enrichment in LREE relative to HREE. This metasomatism is attributed to percolation by a hydrous LILE–K–P–Cr-rich melt, which may be genetically related with the ultrapotassic magmas of the durbachite series. These geochemical characteristics are in line with whole-rock Nd isotopic compositions, which indicate enrichment of the mantle by a continental crust component. Further work is however needed to constrain the precise timing of metasomatic events, understand the exhumation mechanisms of the mantle enclaves and establish more precise correlations with the Variscan magmatic and tectono-metamorphic evolution in the ECM.

Supplementary Material

Figure S1. P–T phase diagram with selected composition isopleths in sample JB-19-33 (garnet lherzolite).

Table S1. Complete set of *in situ* electron microprobe analyses of minerals.

Table S2. Complete set of whole-rock geochemical data, including raw data and data recalculated to an anhydrous basis.

The Supplementary Material is available at http://www.bsgf.fr/10.1051/bsgf/2022021/olm.

References

Ackerman L, Kotková J, Čopjaková R, Sláma J, Trubač J, Dillingerová V. 2020. Petrogenesis and Lu–Hf dating of (ultra) mafic rocks from the Kutná Hora Crystalline Complex: Implications for the Devonian evolution of the Bohemian Massif. *Journal of Petrology.* https://doi.org/10.1093/petrology/egaa075.

Altherr R. 2021. Retrograded garnet peridotites from Col des Bagenelles and Crébimont in the Variscan Vosges Mountains (NE France). *Contributions to Mineralogy and Petrology* 176(7): 53. https://doi.org/10.1007/s00410-021-01811-7.

Altherr R, Kalt A. 1996. Metamorphic evolution of ultrahigh-pressure garnet peridotites from the Variscan Vosges Mountains (France). *Chemical Geology* 134(1): 27–47. https://doi.org/10.1016/S0009-2541(96)00088-5.

Altherr R, Soder CG. 2018. Sapphirine as a breakdown product of garnet in a Variscan UHP/HT Peridotite from the Vosges Mountains (France) – An indication of near-isothermal decompression. *Journal of Petrology* 59(11): 2221–2243. https://doi.org/10.1093/petrology/egy096.

Ballèvre M, Martínez Catalán JR, López-Carmona A, Pitra P, Abati J, Díez Fernández R, *et al.* 2014. Correlation of the nappe stack in the Ibero-Armorican arc across the Bay of Biscay: a joint French–Spanish project. *Geological Society, London, Special Publications* 405: 77–113. https://doi.org/10.1144/SP405.13.

Baier J, Audétat A, Keppler H. 2008. The origin of the negative niobium tantalum anomaly in subduction zone magmas. *Earth and Planetary Science Letters* 267(1): 290–300. https://doi.org/10.1016/j.epsl.2007.11.032.

Barféty JC, Pêcher A. 1984. Geological map and explanatory text of the sheet n 822 "St Christophe en Oisans", Scale: 1:50 000. Ed. BRGM.

Barfety JC, Gidon M, Ménot RP, Debon F, Pêcher S, Guillot S. 2000. Notice de la carte géologique de la France, feuille Domène (773), Scale 1: 50 000. Orléans : BRGM.

Batanova VG, Sobolev AV, Kuzmin DV. 2015. Trace element analysis of olivine: High precision analytical method for JEOL JXA-8230 electron probe microanalyser. *Chemical Geology* 419: 149–157. https://doi.org/10.1016/j.chemgeo.2015.10.0.

Batanova VG, Thompson JM, Danyushevsky LV, Portnyagin MV, Garbe-Schönberg D, Hauri E, *et al.* 2019. New olivine reference material for *in situ* microanalysis. *Geostandards and Geoanalytical Research* 43(3): 453–473. https://doi.org/10.1111/ggr.12266.

Bellahsen N, Mouthereau F, Boutoux A, Bellanger M, Lacombe O, Jolivet L, *et al.* 2014. Collision kinematics in the western external Alps. *Tectonics* 33(6): 1055–1088. https://doi.org/10.1002/2013TC003453.

Bellanger M, Augier R, Bellahsen N, Jolivet L, Monié P, Baudin T, *et al.* 2015. Shortening of the European Dauphinois Margin (Oisans Massif, Western Alps): New insights from RSCM maximum temperature estimates and $^{40}Ar/^{39}Ar$ *in situ* dating. *Journal of Geodynamics* 83: 37–64. https://doi.org/10.1016/j.jog.2014.09.004.

Beyssac O, Goffé B, Chopin C, Rouzaud JN. 2002. Raman spectra of carbonaceous material in metasediments: A new geothermometer. *Journal of Metamorphic Geology* 20: 859–871.

Borghini A, Ferrero S, Wunder B, Laurent O, O'Brien PJ, Ziemann MA. 2018. Granitoid melt inclusions in orogenic peridotite and the origin of garnet clinopyroxenite. *Geology* 46(11): 1007–1010. https://doi.org/10.1130/G45316.1.

Borghini A, Ferrero S, O'Brien PJ, Laurent O, Günter C, Ziemann MA. 2020. Cryptic metasomatic agent measured *in situ* in Variscan mantle rocks: Melt inclusions in garnet of eclogite, Granulitgebirge, Germany. *Journal of Metamorphic Geology* 38(3): 207–234. https://doi.org/10.1111/jmg.12519.

Bouvier A, Vervoort JD, Patchett PJ. 2008. The Lu–Hf and Sm–Nd isotopic composition of CHUR: Constraints from unequilibrated chondrites and implications for the bulk composition of terrestrial planets. *Earth and Planetary Science Letters* 273(1-2): 48–57.

Brey GP, Köhler T. 1990. Geothermobarometry in four-phase Lherzolites II. New thermobarometers, and practical assessment of existing thermobarometers. *Journal of Petrology* 31(6): 1353–1378. https://doi.org/10.1093/petrology/31.6.1353.

Brueckner H. 2018. The great eclogite debate of the Western Gneiss Region, Norwegian Caledonides: The *in situ* crustal *vs.* exotic mantle origin controversy. *Journal of Metamorphic Geology* 36(5): 517–527. https://doi.org/10.1111/jmg.12314.

Brueckner H, Medaris LG. 2000. A general model for the intrusion and evolution of "mantle" garnet peridotites in high-pressure and ultra-high-pressure metamorphic terranes: Intrusion and evolution of 'mantle' garnet peridotites. *Journal of Metamorphic Geology* 18 (2): 123–133. https://doi.org/10.1046/j.1525-1314.2000.00250.x.

Brueckner HK, Carswell DA, Griffin WL, Medaris LG, Van Roermund HLM, Cuthbert SJ. 2010. The mantle and crustal evolution of two garnet peridotite suites from the Western Gneiss Region, Norwegian Caledonides: An isotopic investigation. *Lithos* 117(1): 1–19. https://doi.org/10.1016/j.lithos.2010.01.011.

Carignan J, Hild P, Mevelle G, Morel J, Yeghicheyan D. 2001. Routine analyses of trace elements in geological samples using flow injection and low pressure on-line liquid chromatography coupled to ICP-MS: A study of geochemical reference materials BR, DR-N, UB-N, AN-G and GH. *Geostandards Newsletter* 25 (2-3): 187–198. https://doi.org/10.1111/j.1751-908X.2001.tb00595.x.

Carlson WD. 2006. Rates of Fe, Mg, Mn, and Ca diffusion in garnet. *American Mineralogist* 91(1): 1–11. https://doi.org/10.2138/am.2006.2043.

Chen Y, Su B, Guo S. 2015. The Dabie–Sulu orogenic peridotites: Progress and key issues. *Science China Earth Sciences* 58(10): 1679–1699. https://doi.org/10.1007/s11430-015-5148-9.

Cherniak DJ, Dimanov A. 2010. Diffusion in pyroxene, mica and amphibole. *Reviews in Mineralogy and Geochemistry* 72(1): 641–690. https://doi.org/10.2138/rmg.2010.72.14.

Connolly JAD. 2009. The geodynamic equation of state: What and how. *Geochemistry, Geophysics, Geosystems* 10(10). https://doi.org/10.1029/2009GC002540.

Debon F, Lemmet M. 1999. Evolution of Mg/Fe ratios in Late Variscan Plutonic rocks from the External Crystalline Massifs of the Alps (France, Italy, Switzerland). *Journal of Petrology* 40(7): 1151–1185. https://doi.org/10.1093/petroj/40.7.1151.

Debon F, Guerrot C, Ménot R-P. 1998. Late Variscan granites of the Belledonne Massif (French Western Alps): An Early Visean magnesian plutonism. *Schweizerische Mineralogische Und Petrographische Mitteilungen* 78: 67–85. https://doi.org/10.5169/seals-59275.

Deschamps F, Godard M, Guillot S, Hattori K. 2013. Geochemistry of subduction zone serpentinites: A review. *Lithos* 178: 96–127. https://doi.org/10.1016/j.lithos.2013.05.019.

Duesterhoeft E, Lanari P. 2020. Iterative thermodynamic modelling – Part 1: A theoretical scoring technique and a computer program (Bingo-Antidote). *Journal of Metamorphic Geology* 38(5): 527–551. https://doi.org/10.1111/jmg.12538.

Faure M, Lardeaux J-M, Ledru P. 2009. A review of the pre-Permian geology of the Variscan French Massif Central. *Comptes Rendus Geoscience* 341(2-3): 202–213.

Ferrando S, Lombardo B, Compagnoni R. 2008. Metamorphic history of HP mafic granulites from the Gesso-Stura terrain (Argentera Massif, Western Alps, Italy). *European Journal of Mineralogy* 20(5): 777–790.

Foley SF, Pertermann M. 2021. Dynamic metasomatism experiments investigating the interaction between migrating potassic melt and garnet peridotite. *Geosciences* 11(10): article 10. https://doi.org/10.3390/geosciences11100432.

Foley SF, Venturelli G, Green DH, Toscani L. 1987. The ultrapotassic rocks: Characteristics, classification, and constraints for petrogenetic models. *Earth-Science Reviews* 24(2): 81–134. https://doi.org/10.1016/0012-8252(87)90001-8.

Fréville K, Trap P, Faure M, Melleton J, Li X-H, Lin W, *et al.* 2018. Structural, metamorphic and geochronological insights on the Variscan evolution of the Alpine basement in the Belledonne Massif (France). *Tectonophysics* 726: 14–42.

Fréville K, Trap P, Vanardois J, Melleton J, Faure M, Bruguier O, *et al.* 2022. Carboniferous-Permian tectono-metamorphic evolution of the Pelvoux Massif (External Crystalline Massif, Western Alps), with discussion on flow kinematics of the Eastern-Variscan Shear Zone. *Bulletin de la Société Géologique de France* 193(1): 13. https://doi.org/10.1051/bsgf/2022008.

Gardien V, Tegyey M, Lardeaux JM, Misseri M, Dufour E. 1990. Crust-mantle relationships in the French Variscan chain: The example of the Southern Monts du Lyonnais unit (Eastern French Massif Central). *Journal of Metamorphic Geology* 8(5): 477–492. https://doi.org/10.1111/j.1525-1314.1990.tb00481.x.

Godard G. 1990. Découverte d'éclogites, de péridotites à spinelle et d'amphibolites à anorthite, spinelle et corindon. *Comptes Rendus de l'Académie Des Sciences. Série 2, Mécanique, Physique, Chimie, Sciences de l'univers, Sciences de la Terre* 310(3): 227–232.

Godard G, Martin S. 2000. Petrogenesis of kelyphites in garnet peridotites: A case study from the Ulten Zone, Italian Alps. *Journal of Geodynamics* 30(1): 117–145. https://doi.org/10.1016/S0264-3707(99)00030-7.

Godard G, Martin S, Prosser G, Kienast JR, Morten L. 1996. Variscan migmatites, eclogites and garnet-peridotites of the Ulten Zone, Eastern Austroalpine system. *Tectonophysics* 259(4): 313–341. https://doi.org/10.1016/0040-1951(95)00145-X.

Grandjean V, Guillot S, Pecher A. 1996. A new record of the LP-HT Late Variscan metamorphism: The Peyre-Arguet unit (Haut-Dauphine). *Comptes Rendus de l'Académie des sciences* 322: 189–195.

Guillot S, Ménot R. 1999. Nappe stacking and first evidence of Late Variscan extension in the Belledonne Massif (External Crystalline Massifs, French Alps). *Geodinamica Acta* 12: 97–111. https://doi.org/10.1016/S0985-3111(99)80026-6.

Guillot S, Ménot R-P. 2009. Paleozoic evolution of the External Crystalline Massifs of the Western Alps. *Comptes Rendus Geoscience* 341(2-3): 253–265. https://doi.org/10.1016/j.crte.2008.11.010.

Guillot S, Hattori K, Agard P, Schwartz S, Vidal O. 2009. Exhumation processes in oceanic and continental subduction contexts: A review. *Subduction Zone Geodynamics*: 175–205.

Hermann J, Rubatto D. 2009. Accessory phase control on the trace element signature of sediment melts in subduction zones. *Chemical Geology* 265(3): 512–526. https://doi.org/10.1016/j.chemgeo.2009.05.018.

Holland TJB, Powell R. 2011. An improved and extended internally consistent thermodynamic dataset for phases of petrological interest, involving a new equation of state for solids. *Journal of Metamorphic Geology* 29(3): 333–383. https://doi.org/10.1111/j.1525-1314.2010.00923.x.

Ionov DA, Wood BJ. 1992. The oxidation state of subcontinental mantle: Oxygen thermobarometry of mantle xenoliths from Central Asia. *Contributions to Mineralogy and Petrology* 111(2): 179–193.

Jacob J-B, Guillot S, Rubatto D, Janots E, Melleton J, Faure M. 2021. Carboniferous high pressure metamorphism and deformation in the Belledonne Massif (Western Alps). *Journal of Metamorphic Geology* n/a(n/a). https://doi.org/10.1111/jmg.12600.

Jacob J-B, Janots E, Guillot S, Rubatto D, Fréville K, Melleton J, *et al.* 2022. HT overprint of HP granulites in the Oisans–Pelvoux Massif: Implications for the dynamics of the Variscan collision in the external Western Alps. *Lithos* 416-417: 106650. https://doi.org/10.1016/j.lithos.2022.106650.

Jagoutz E, Palme H, Baddenhausen H, *et al.* 1979. The abundances of major, minor and trace elements in the earth's mantle as derived from primitive ultramafic nodules. In: *Lunar and Planetary Science Conference Proceedings*, pp. 2031–2050.

Janoušek V, Holub FV. 2007. The causal link between HP–HT metamorphism and ultrapotassic magmatism in collisional orogens: Case study from the Moldanubian Zone of the Bohemian Massif. *Proceedings of the Geologists' Association* 118(1): 75–86. https://doi.org/10.1016/S0016-7878(07)80049-6.

Janoušek V, Moyen J-F, Martin H, Erban V, Farrow C. 2016. Classical plots. In: Janoušek V, Moyen J-F, Martin H, Erban V, Farrow C, eds. *Geochemical Modelling of Igneous Processes – Principles And Recipes in R Language: Bringing the Power of R to a Geochemical Community* (pp. 27–43). Springer. https://doi.org/10.1007/978-3-662-46792-3_3.

Janoušek V, Bonin B, Collins WJ, Farina F, Bowden P. 2019. Post-Archean granitic rocks: Contrasting petrogenetic processes and tectonic environments. Geological Society of London.

Janoušek V, Hanžl P, Svojtka M, Hora JM, Kochergina YVE, Gadas P, *et al.* 2020. Ultrapotassic magmatism in the heyday of the Variscan Orogeny: The story of the Třebíč Pluton, the largest durbachitic body in the Bohemian Massif. *International Journal of Earth Sciences* 109 (5): 1767–1810. https://doi.org/10.1007/s00531-020-01872-2.

Jarosewich E, Nelen JA, Norberg JA. 1980. Reference samples for electron microprobe analysis. *Geostandards Newsletter* 4(1): 43–47.

Jennings ES, Holland TJB. 2015. A simple thermodynamic model for melting of peridotite in the system NCFMASOCr. *Journal of Petrology* 56(5): 869–892. https://doi.org/10.1093/petrology/egv020.

Jouffray F, Spalla MI, Lardeaux JM, Filippi M, Rebay G, Corsini M, *et al.* 2020. Variscan eclogites from the Argentera–Mercantour Massif (External Crystalline Massifs, SW Alps): A dismembered cryptic suture zone. *International Journal of Earth Sciences*. https://doi.org/10.1007/s00531-020-01848-2.

Kotková J, O'Brien PJ, Ziemann MA. 2011. Diamond and coesite discovered in Saxony-type granulite: Solution to the Variscan garnet peridotite enigma. *Geology* 39(7): 667–670. https://doi.org/10.1130/G31971.1.

Kubeš M, Leichmann J, Kotková J, Čopjaková R, Holá M, Sláma J. 2022. Diversity of origin and geodynamic evolution of the mantle beneath the Variscan Orogen indicating rapid exhumation within subduction-related mélange (Moldanubian Zone, Bohemian Massif). *Lithos* 422-423: 106726. https://doi.org/10.1016/j.lithos.2022.106726.

Lardeaux JM, Schulmann K, Faure M, Janoušek V, Lexa O, Skrzypek E, *et al.* 2014. The moldanubian zone in the French Massif Central, Vosges/Schwarzwald and Bohemian Massif revisited: Differences and similarities. *Geological Society, London, Special Publications* 405(1): 7–44.

Le Fort P. 1971. Géologie du Haut-Dauphiné cristallin (Alpes Française) : Études pétrologique et structurale de la partie occidentale. PhD Thesis, Université Nancy I.

Lexa O, Schulmann K, Janoušek V, Štípská P, Guy A, Racek M. 2011. Heat sources and trigger mechanisms of exhumation of HP granulites in Variscan orogenic root: Heat sources and exhumation mechanisms. *Journal of Metamorphic Geology* 29(1): 79–102. https://doi.org/10.1111/j.1525-1314.2010.00906.x.

Luais B, Telouk P, Albaréde F. 1997. Precise and accurate neodymium isotopic measurements by plasma-source mass spectrometry. *Geochimica et Cosmochimica Acta* 61(22): 4847–4854.

Lugmair GW, Marti K. 1978. Lunar initial $^{143}Nd/^{144}Nd$: Differential evolution of the lunar crust and mantle. *Earth and Planetary Science Letters* 39(3): 349–357.

Maierová P, Schulmann K, Gerya T. 2018. Relamination styles in collisional orogens. *Tectonics* 37(1): 224–250. https://doi.org/10.1002/2017TC004677.

Maierová P, Schulmann K, Štípská P, Gerya T, Lexa O. 2021. Trans-lithospheric diapirism explains the presence of ultra-high pressure rocks in the European Variscides. *Communications Earth & Environment* 2(1): 56. https://doi.org/10.1038/s43247-021-00122-w.

Malaspina N, Hermann J, Scambelluri M, Compagnoni R. 2006. Polyphase inclusions in garnet–orthopyroxenite (Dabie Shan, China) as monitors for metasomatism and fluid-related trace element transfer in subduction zone peridotite. *Earth and Planetary Science Letters* 249(3): 173–187. https://doi.org/10.1016/j.epsl.2006.07.017.

Malatesta C, Crispini L, Federico L, Capponi G, Scambelluri M. 2012. The exhumation of high pressure ophiolites (Voltri Massif, Western Alps): Insights from structural and petrologic data on metagabbro bodies. *Tectonophysics* 568-569: 102–123. https://doi.org/10.1016/j.tecto.2011.08.024.

Martínez Catalán JR, Schulmann K, Ghienne J-F. 2021. The Mid-Variscan Allochthon: Keys from correlation, partial retrodeformation and plate-tectonic reconstruction to unlock the geometry of a non-cylindrical belt. *Earth-Science Reviews* 220: 103700. https://doi.org/10.1016/j.earscirev.2021.103700.

McDonough WF, Sun S-S. 1995. The composition of the Earth. *Chemical Geology* 120: 223–253. https://doi.org/10.1016/0009-2541(94)00140-4.

Medaris G, Wang H, Jelínek E, Mihaljevič M, Jakeš P. 2005. Characteristics and origins of diverse Variscan peridotites in the Gföhl Nappe, Bohemian Massif, Czech Republic. *Lithos* 82(1): 1–23. https://doi.org/10.1016/j.lithos.2004.12.004.

Medaris G, Ackerman L, Jelínek E, Michels ZD, Erban V, Kotková J. 2015. Depletion, cryptic metasomatism, and modal metasomatism (refertilization) of Variscan lithospheric mantle: Evidence from major elements, trace elements, and Sr–Nd–Os isotopes in a Saxothuringian garnet peridotite. *Lithos* 226: 81–97. https://doi.org/10.1016/j.lithos.2014.10.007.

Ménot R-P, Peucat JJ, Scarenzi D, Piboule M. 1988. 496 My age of plagiogranites in the Chamrousse ophiolite complex (external crystalline massifs in the French Alps): Evidence of a Lower Paleozoic oceanization. *Earth and Planetary Science Letters* 88(1-2): 82–92.

Moyen J-F, Laurent O, Chelle-Michou C, Couzinié S, Vanderhaeghe O, Zeh A, *et al.* 2017. Collision *vs.* subduction-related magmatism: Two contrasting ways of granite formation and implications for crustal growth. *Lithos* 277: 154–177. https://doi.org/10.1016/j.lithos.2016.09.018.

Nickel KG, Green DH. 1985. Empirical geothermobarometry for garnet peridotites and implications for the nature of the lithosphere, kimberlites and diamonds. *Earth and Planetary Science Letters* 73 (1): 158–170. https://doi.org/10.1016/0012-821X(85)90043-3.

Nimis P, Trommsdorff V. 2001. Revised thermobarometry of Alpe Arami and other Garnet Peridotites from the Central Alps. *Journal of Petrology* 42(1): 103–115. https://doi.org/10.1093/petrology/42.1.103.

Nimis P, Grütter H. 2010. Internally consistent geothermometers for garnet peridotites and pyroxenites. *Contributions to Mineralogy and Petrology* 159(3): 411–427. https://doi.org/10.1007/s00410-009-0455-9.

Nouibat A, Stehly L, Paul A, Schwartz S, Bodin T, Dumont T, *et al.* 2022. Lithospheric transdimensional ambient-noise tomography of W- Europe: Implications for crustal-scale geometry of the W-Alps. *Geophysical Journal International* 229(2): 862–879. https://doi.org/10.1093/gji/ggab520.

Obata M. 2011. Kelyphite and symplectite: Textural and mineralogical diversities and universality, and a new dynamic view of their structural formation. In: Sharkov E, ed. *New Frontiers in Tectonic Research – General Problems, Sedimentary Basins and Island Arcs*. InTech. https://doi.org/10.5772/20265.

Paquette JL, Ménot RP, Peucat JJ. 1989. REE, Sm–Nd and U–Pb zircon study of eclogites from the Alpine External Massifs (Western Alps): Evidence for crustal contamination. *Earth and Planetary Science Letters* 96(1-2): 181–198.

Paulick H, Bach W, Godard M, De Hoog JCM, Suhr G, Harvey J. 2006. Geochemistry of abyssal peridotites (Mid-Atlantic Ridge, 15.20′N, ODP Leg 209): Implications for fluid/rock interaction in slow spreading environments. *Chemical Geology* 234(3-4): 179–210. https://doi.org/10.1016/j.chemgeo.2006.04.011.

Pecher A. 1970. Étude pétrographique de la partie orientale du massif des Écrins–Pelvoux : Le socle ancien – Alpes françaises. https://tel.archives-ouvertes.fr/tel-00576930.

Perraki M, Faryad SW. 2014. First finding of microdiamond, coesite and other UHP phases in felsic granulites in the Moldanubian Zone: Implications for deep subduction and a revised geodynamic model for Variscan Orogeny in the Bohemian Massif. *Lithos* 202-203: 157–166. https://doi.org/10.1016/j.lithos.2014.05.025.

Pin C, Carme F. 1987. A Sm-Nd isotopic study of 500 Ma old oceanic crust in the Variscan Belt of Western Europe: The Chamrousse ophiolite complex, Western Alps (France). *Contributions to Mineralogy and Petrology* 96(3): 406–413.

Pin C, Zalduegui JS. 1997. Sequential separation of light rare-earth elements, thorium and uranium by miniaturized extraction chromatography: Application to isotopic analyses of silicate rocks. *Analytica Chimica Acta* 339(1-2): 79–89.

Pin C, Briot D, Bassin C, Poitrasson F. 1994. Concomitant separation of strontium and samarium-neodymium for isotopic analysis in silicate samples, based on specific extraction chromatography. *Analytica Chimica Acta* 298(2): 209–217.

Rubatto D, Ferrando S, Compagnoni R, Lombardo B. 2010. Carboniferous high-pressure metamorphism of Ordovician proto-liths in the Argentera Massif (Italy), Southern European Variscan Belt. *Lithos* 116(1-2): 65–76.

Ruiz M, Schaltegger U, Gaynor SP, Chiaradia M, Abrecht J, Gisler C, *et al.* 2022. Reassessing the intrusive tempo and magma genesis of the late Variscan Aar batholith: U–Pb geochronology, trace element and initial Hf isotope composition of zircon. *Swiss Journal of Geosciences* 115(1): 20. https://doi.org/10.1186/s00015-022-00420-1.

Sapienza GT, Scambelluri M, Braga R. 2009. Dolomite-bearing orogenic garnet peridotites witness fluid-mediated carbon recycling in a mantle wedge (Ulten Zone, Eastern Alps, Italy). *Contributions to Mineralogy and Petrology* 158(3): 401–420. https://doi.org/10.1007/s00410-009-0389-2.

Scambelluri M, Hermann J, Morten L, Rampone E. 2006. Melt-versus fluid-induced metasomatism in spinel to garnet wedge peridotites (Ulten Zone, Eastern Italian Alps): Clues from trace element and Li abundances. *Contributions to Mineralogy and Petrology* 151(4): 372–394. https://doi.org/10.1007/s00410-006-0064-9.

Schulmann K, Konopásek J, Janoušek V, Lexa O, Lardeaux J-M, Edel J-B, *et al.* 2009. An Andean type Palaeozoic convergence in the Bohemian Massif. *Comptes Rendus Geoscience* 341: 266–286. https://doi.org/10.1016/j.crte.2008.12.006.

Schulmann K, Catalán J-RM, Lardeaux J-M, Janoušek V, Oggiano G. 2014. The Variscan orogeny: Extent, timescale and the formation of the European crust. *Geological Society, London, Special Publications* 405(1): 1–6. https://doi.org/10.1144/SP405.15.

Schulmann K, Lexa O, Janoušek V, Lardeaux J-M, Edel J-B. 2014. Anatomy of a diffuse cryptic suture zone: An example from the Bohemian Massif, European Variscides. *Geology* 42(4): 275–278. https://doi.org/10.1130/G35290.1.

Skrzypek E, Štípská P, Cocherie A. 2012. The origin of zircon and the significance of U–Pb ages in high-grade metamorphic rocks: A case study from the Variscan orogenic root (Vosges Mountains, NE France). *Contributions to Mineralogy and Petrology* 164(6): 935–957. https://doi.org/10.1007/s00410-012-0781-1.

Sobolev AV, Hofmann AW, Kuzmin DV, Yaxley GM, Arndt NT, Chung S-L, *et al.* 2007. The amount of recycled crust in sources of mantle-derived melts. *Science* 316(5823): 412–417. https://doi.org/10.1126/science.1138113.

Soder CG, Romer RL. 2018. Post-collisional Potassic–Ultrapotassic Magmatism of the Variscan Orogen: Implications for Mantle Metasomatism during Continental Subduction. *Journal of Petrology* 59(6): 1007–1034. https://doi.org/10.1093/petrology/egy053.

Steiger RH, Jäger E. 1977. Subcommission on geochronology: Convention on the use of decay constants in geo- and cosmochronology. *Earth and Planetary Science Letters* 36(3): 359–362. https://doi.org/10.1016/0012-821X(77)90060-7.

Tanaka T, Togashi S, Kamioka H, Amakawa H, Kagami H, Hamamoto T, *et al.* 2000. JNdi-1: A neodymium isotopic reference in consistency with LaJolla neodymium. *Chemical Geology* 168 (3-4): 279–281.

Taylor WR. 1998. An experimental test of some geothermometer and geobaro-meter formulations for upper mantle peridotites with application to the ther-mobarometry of fertile lherzolite and garnet websterite. *Neues Jahrbuch Für Mineralogie – Abhandlungen*: 381–408. https://doi.org/10.1127/njma/172/1998/381.

Tumiati S, Thöni M, Nimis P, Martin S, Mair V. 2003. Mantle-crust interactions during Variscan subduction in the Eastern Alps (Nonsberg-Ulten Zone): Geochronology and new petrological constraints. *Earth and Planetary Science Letters* 210(3-4): 509–526.

Vanardois J, Roger F, Trap P, Goncalves P, Lanari P, Paquette J-L, *et al.* 2022. Exhumation of deep continental crust in a transpressive regime: The example of Variscan eclogites from the Aiguilles-Rouges Massif (Western Alps). *Journal of Metamorphic Geology.*

Vanderhaeghe O, Laurent O, Gardien V, Moyen J-F, Gébelin A, Chelle-Michou C, *et al.* 2020. Flow of partially molten crust controlling construction, growth and collapse of the Variscan orogenic belt: The geologic record of the French Massif Central. *Bulletin de la Société Géologique de France* 191(25). https://doi.org/10.1051/bsgf/2020013.

Von Raumer JF, Bussy F. 2004. Mont Blanc and Aiguilles Rouges geology of their polymetamorphic basement (external massifs, Westerns Alps, France-Switzerland). *Mémoires de Géologie (Lausanne)* 42: 1–210.

Von Raumer JF, Stampfli GM. 2008. The birth of the Rheic Ocean – Early Palaeozoic subsidence patterns and subsequent tectonic plate scenarios. *Tectonophysics* 461(1-4): 9–20.

Von Raumer JF, Finger F, Veselá P, Stampfli GM. 2014. Durbachites–Vaugnerites – A geodynamic marker in the Central European Variscan orogen. *Terra Nova* 26(2): 85–95.

Wang J-M, Lanari P, Wu F-Y, Zhang J-J, Khanal GP, Yang L. 2021. First evidence of eclogites overprinted by ultrahigh temperature metamorphism in Everest East, Himalaya: Implications for collisional tectonics on early Earth. *Earth and Planetary Science Letters* 558: 116760. https://doi.org/10.1016/j.epsl.2021.116760.

Zheng Y-F. 2019. Subduction zone geochemistry. *Geoscience Frontiers* 10(4): 1223–1254. https://doi.org/10.1016/j.gsf.2019.02.003.

Ziberna L, Klemme S, Nimis P. 2013. Garnet and spinel in fertile and depleted mantle: Insights from thermodynamic modelling. *Contributions to Mineralogy and Petrology* 166(2): 411–421. https://doi.org/10.1007/s00410-013-0882-5.